Joint Features Extraction for Multiple Moving Targets Using (Ultra-)Wideband FMCW Signals in the Presence of Doppler Ambiguity

Xu, Shengzhi; Yarovoy, Alexander

DOI
10.1109/TSP.2020.3039565

Publication date
2020

Document Version
Final published version

Published in
IEEE Transactions on Signal Processing

Joint Features Extraction for Multiple Moving Targets Using (Ultra-)Wideband FMCW Signals in the Presence of Doppler Ambiguity

Shengzhi Xu and Alexander Yarovoy, *Fellow, IEEE*

***Abstract*—This article addresses the joint estimation of range, velocity and azimuth for multiple fast-moving targets using (ultra-)wideband (UWB) frequency-modulated continuous-wave (FMCW) radar with a phased array in the presence of Doppler ambiguities. The range migration of moving targets is described with the coupling of the fast-time and slow-time (chirp index), leading to the smearing of the target Doppler spectrum. This phenomenon degrades the performance of conventional detection and estimation techniques. As with range-Doppler processing, the estimation accuracy for direction-of-arrival (DOA) with conventional narrowband-based algorithms significantly degrades if a UWB signal is deployed. For the FMCW waveform, the wideband DOA differs from the narrowband DOA due to an extra coupling term, similar to the range migration problem. A novel spectral norm-based algorithm for joint estimation of range, velocity and DOA of fast-moving targets is proposed, taking the appropriate wideband signal model with the coupling terms into account. The proposed spectral norm-based algorithm avoids off-grid peak search and can be easily accelerated with power iteration; it outperforms conventional coherent integration methods in both accuracy and efficiency when using moderate data size. The advantages of the proposed algorithm and its super-resolution capability are validated with numerical simulations.**

***Index Terms*—(ultra-)wideband, DOA, doppler ambiguities, FMCW, power iteration.**

I. Introduction

(ULTRA-)WIDEBAND (UWB) radar technology for moving target detection and location has evolved over the past decades in diverse fields due to a demand for increasingly higher range resolution [1]–[3]. In addition to the need for high range resolution, an accurate estimation of the Doppler velocity and DOA of multiple moving targets is required in many applications, e.g. in autonomous driving using radar sensors. However, the small range cell size of UWB radars leads to a range migration phenomenon in which a fast-moving target passes several range cells during the coherent processing interval (CPI). Mathematically, the range migration introduces the coupling term between the fast-time and slow-time domains [4], [5], which within classical Fourier-based Doppler processing leads to the spreading of the target response in the range-Doppler plane and, consequently, degradation in target detection and tracking. Many algorithms have been proposed to mitigate range migration problems, such as the Keystone algorithm via data interpolation [6], the RELAX method [7] and compensated MUSIC [8]. Simultaneously, the coupled data offer the possibility to resolve the Doppler ambiguity fold number (Doppler ambiguity index) [9].

According to the Nyquist sampling criterion, there exists a maximum unambiguous velocity, which is determined by the constant pulse repetition frequency (PRF). When the target radial velocity is larger than the maximum unambiguous velocity, it is folded into the unambiguous domain of the Doppler spectrum. This problem is common to the low PRF waveforms. Although some waveform design techniques for unambiguous estimation of Doppler and range have been proposed, such as multiple pulse repetition frequencies (MPRF) combined with Chinese Remainder Theorem (CRT) [10] or up-/down-chirps [11], these approaches increase the system complexity and perform unsatisfactorily under low signal to noise ratio (SNR) conditions.

For single PRF waveforms, several approaches for unambiguous Doppler frequency estimation using the range migration coupling term have been proposed [9], [12]–[26]. These methods can be roughly divided into three categories: parametric methods, incoherent integration-based and coherent integration-based methods. The parametric methods use the noise covariance matrix model and solve the problem with the Bayes estimator [12]–[14]. In addition to the heavy computational load, these methods are also usually sensitive to parameter settings and initialisation. Incoherent integration methods, for instance, Hough transform (HT) [15], suffer from poor performance under low SNR conditions. Coherent methods are usually performed usingthe matched filter (MF) bank, e.g., W-Capon, W-APES [16], time-reversing transform [17], [18], scaled inverse Fourier transform [19], modified location rotation transform [20] and iterative adaptive algorithm (IAA), the latter of which is extended to wideband waveforms [9]. Keystone transform along with some focussing criteria can also be applied to the unambiguous velocity extraction [21]–[23]. Another famous coherent integration method is Radon Fourier transform (RFT) achieved by the coupling term compensation and coherent

Manuscript received April 12, 2019; revised November 18, 2019, September 23, 2020, and November 12, 2020; accepted November 16, 2020. Date of publication November 23, 2020; date of current version December 3, 2020. The associate editor coordinating the review of this manuscript and approving it for publication was Dr. Mariane R. Petraglia. *(Corresponding author: Shengzhi Xu.)*

The authors are with the MS3, Delft University of Technology, 2628 CD Delft, The Netherlands (e-mail: sz.xu@hotmail.com; A.Yarovoy@tudelft.nl).

Digital Object Identifier 10.1109/TSP.2020.3039565

integration. It is shown in [24]–[26] that generalised RFT is the optimal coherent integration-based method for rectilinearly moving targets under a background of white Gaussian noise. However, to accurately resolve the Doppler ambiguity via interpolation or coherent integration, these approaches usually need a large data size, which is often unavailable due to limited observation time. Moreover, without appropriate grid oversampling, MF suffers from collapsing loss in off-grid targets. Moderate oversampling in every dimension is required to overcome this problem, but this comes with an increased computational burden.

In addition to range migration, another challenge of wideband signals is estimating DOA using collocated array or MIMO antenna array. Traditional DOA estimators are based on narrowband assumptions of interferometry information, such as Delay-and-Sum (DAS), Capon, MUSIC [27], variational Bayesian-based approaches [28], [29] and greedy-based approach [30]. They cannot be directly applied to the wideband case because the actual steering vector determined by the wavelength varies with frequency, which consequently reduces the accuracy of DOA estimations with the narrowband estimators. Current solutions for wideband DOA estimation include the incoherent signal subspace method (ISSM) and the coherent signal subspace method (CSSM) [31]. However, these algorithms are general wideband DOA solutions and are either computationally complex or sensitive to noise level and initial guess [32]. In previous studies, the range migration problem (mitigation or ambiguous Doppler estimation) has typically been addressed separately from the wideband DOA estimation problem. Joint treatment of the range migration and wideband DOA estimation is essential for multiple moving targets, as this resolves the target association problem and helps to improve SNR through the simultaneous processing of the entire data cube (fast-time, slow-time and antenna array element). In our previous study [4], wideband DOA and range migration were treated simultaneously without the presence of Doppler ambiguity. This paper presents a novel approach to addressing the problem of feature extraction (range, Doppler, DOA) of multiple moving targets in the presence of Doppler ambiguity. The signal model is developed based on the FMCW waveform, for which the wideband DOA problem can be decomposed into the narrowband signal model with an extra second-order inter-coupling component. By doing this, the range migration and wideband DOA are described similarly as second-order coupling terms and can be processed analogously. A novel spectral norm-based algorithm is proposed to address both problems together. Certainly, the same algorithm can also be applied to two-dimensional coupling problems, for instance, range-Doppler processing, which addresses the range migration issue.

There are 6 algorithms listed in this paper ($\mathbf{A}1 \backsim \mathbf{A}6$), and the main novelties of this paper are summarised as follows:

1) An accurate signal model is established and analysed which, for the first time, takes both wideband DOA and ambiguous Doppler estimation into account simultaneously.
2) The spectral norm-based algorithm introduced in $\mathbf{A}2$ is based on a principally new approach and does not belong to any existing category of algorithms, since it is a non-parametric and non-integration based algorithm. It can be recognised as the fourth category.
3) The coupling terms (range migration and wideband DOA) are addressed separately from the sinusoidal signals corresponding to the range, Doppler and DOA in $\mathbf{A}2$, while the existing algorithms process Doppler ambiguity from the coupling terms and sinusoids together. Moreover, due to the use of alternative updating between the coupling terms and the sinusoids in $\mathbf{A}2$, the convergent condition is relaxed in terms of SNR.
4) The proposed algorithm outperforms the conventional coherent integration-based algorithm in terms of accuracy since it avoids the off-grid problem for the fold number estimation.
5) By introducing an efficient implementation via the proposed data reshaping, $\mathbf{A}2$ can be solved with less time- and memory-consumption. Furthermore, $\mathbf{A}6$ is specifically proposed for our algorithm, which provides a more efficient way to solve $\mathbf{A}2$ using power iteration ($\mathbf{A}5$).
6) The performance of the proposed algorithm is analysed in detail for root-mean-square-error (RMSE) of all target parameter estimation and is compared to the corresponding Cramér-Rao Bound (CRB) in different scenarios. Furthermore, the simulation results demonstrate that the proposed algorithm supports the super-resolution ability of RELAX algorithm ($\mathbf{A}4$).

The rest of the paper is organised as follows. In Section II, the signal model for FMCW waveform is established and the problem formulation is provided. In Section III, a novel algorithm for a single moving target is introduced. Subsequently, in Section IV the proposed algorithm is combined with the greedy algorithm and the RELAX estimator. Section V presents an efficient implementation of the proposed algorithm. Numerical examples are presented in Section VI to illustrate the performance of the proposed algorithm and to compare it with CRB. Finally, the conclusions are drawn in Section VII.

Notations used in this paper are as follows. Scalars are denoted with lower-case letters, vectors and matrices are written as lower-case and upper-case bold-face letters, and multi-way tensors are written as bold calligraphic letters, respectively. $(\cdot)^T$, $(\cdot)^H$ and $(\cdot)^*$ denote the transpose, conjugate transpose and complex conjugate of a vector or matrix, respectively. Symbols $\circ$, $\otimes$, $\odot$ and $\times_n$ represent the outer product, Kronecker product, Hadamard product and tensor n-mode product [33], respectively. $\lfloor x \rfloor$ gives the nearest integer less than or equal to x and $\lfloor x \rceil$ returns the nearest integer to x. $||\cdot||_2$ and $||\cdot||_F$ denote the matrix spectral norm and Frobenius norm of a matrix, respectively. The max norm of a matrix or a vector is denoted as $||\cdot||_{\max}$, which returns the entry with the maximum absolute value of a matrix or a vector. $\boldsymbol{\sigma}(\mathbf{A})$ denotes the spectrum of the matrix $\mathbf{A}$; $[\mathbf{A}]_{p,q}$ denotes the entry of matrix $\mathbf{A}$ at the $(p+1)$th row and $(q+1)$th column; $[\boldsymbol{\mathcal{A}}]_{p,q,r}$ denotes the entry of tensor $\boldsymbol{\mathcal{A}}$ at the $(p+1)$th row, $(q+1)$th column and $(r+1)$th tube. This means that the indices of the vector, matrix or tensor in this paper start at 0. $\mathbf{I}_M$ denotes the $M \times M$ identity matrix.

Some other special vectors are $\mathbf{1}_M = [1, 1, \ldots, 1]^T \in \mathbb{R}^{M\times 1}$ and $\mathbf{d}_M = [0, 1, \ldots, M-1]^T \in \mathbb{R}^{M\times 1}$. $\mathcal{U}(a, b)$ denotes the continuous uniform distribution in the interval (a, b). $\mathscr{F}()$, $\mathbb{E}()$, Tr(), $\Re()$ and $\Im()$ represent Fourier transform operation, the expectation operator, the trace of a matrix, and the real and imaginary part extraction operation, respectively.

II. Signal Model And Discussion

In this section, the signal model of a mono-static antenna array with one transmitter and L receivers is formulated. Without losing generality, a uniformly distributed linear array (ULA) with omnidirectional elements is considered for the receivers. The constraint between the maximum unambiguous range, maximum unambiguous velocity and the sampling frequency is then discussed to highlight the challenge of the ambiguous velocity estimation in UWB FMCW waveform.

A. Signal Model

Let us assume I point targets with an unknown initial range $\mathbf{r} = [R_1, R_2, \ldots, R_I]$, radial velocity $\mathbf{v} = [v_1, v_2, \ldots, v_I]$ and angle $\boldsymbol{\theta} = [\theta_1, \theta_2, \ldots, \theta_I]$ are presented in the observation scene and satisfy the far-field condition. During one CPI, a sequence of FMCW chirps is transmitted with the chirp duration T_0 and the pulse repetition interval (PRI) T_r. A normalised single chirp signal with bandwidth B has the form

$$s_0(t) = \begin{cases} e^{j2\pi(f_0 t + 0.5\mu t^2)} & t \in [0, T_0], \\ \text{settle time} & t \in (T_0, T_r), \end{cases} \tag{1}$$

where f_0 is the starting frequency, $\mu = \frac{B}{T_0}$ denotes the frequency modulation rate, and the settle time is the system reset interval. The periodic transmitted signal is decomposed into fast-time domain t' and chirp number (slow-time) domain $m = \lfloor \frac{t}{T_r} \rfloor$ as $t' = t - mT_r,\ t' \in [0, T_r)$, where $m = 0, 1, 2, \ldots, M-1$ and M is the total number of chirps in one CPI.

Then the periodically transmitted signal can be decomposed into fast-time t' and slow-time index m as

$$s(t) = s(t' + mT_r) = s(m, t') = s_0(t'). \tag{2}$$

The ith scatterer in the observation scene with radial velocity v_i and initial range R_i is illuminated by the radar, and the reflected signal arrives back at the radar with the time delay

$$\tau_i(m, t') = \frac{2(R_i + v_i(t' + mT_r))}{c} = \gamma_i + \frac{2v_i}{c}(t' + mT_r), \tag{3}$$

where c is the speed of light and $\gamma_i = \frac{2R_i}{c}$ is the initial round trip delay of the ith scatterer. Using the 0th element of the array as the reference, the received signal of the ith scatterer at the lth element can be written as

$$\begin{aligned} r_i^{(l)}(m, t') &= \alpha_i e^{j\varphi_i^{(l)}} s(t' + mT_r - \tau_i(m, t')) \\ &= \alpha_i e^{j\varphi_i^{(l)}} e^{j2\pi\phi_i(m,t')}, \\ &\text{with } t' \in [\gamma_i, T_0 + \gamma_i], \end{aligned} \tag{4}$$

where the superscript (l) denotes the element index of receiver array with $l = 0, 1, 2, \ldots, L-1$ and L is the total number of receivers, α_i is the constant complex amplitude of the ith scatterer, $\exp(j\varphi_i^{(l)})$ denotes the phase delay relative to the 0th element and, according to (1) and (2), the term $\phi_i(m, t')$ has the form

$$\phi_i(m, t') = f_0(t' - \tau_i(m, t')) + 0.5\mu(t' - \tau_i(m, t'))^2. \tag{5}$$

From the phase of the received signal, the instantaneous frequency of the received signal is extracted as

$$f_i(m, t') = \frac{\partial \phi_i(m, t')}{\partial t'} \approx f_0 + \mu t'. \tag{6}$$

Here the terms of the time delay are ignored because of $\tau_i(m, t') << T_0$ and $v_i << c$. Then the phase delay of the lth element relative to the 0th element is obtained by

$$\begin{aligned} \varphi_i^{(l)} &= 2\pi f_i(m, t')\frac{ld}{c}\sin\theta_i \\ &= 2\pi(f_0 + \mu t')\frac{ld}{c}\sin\theta_i, \end{aligned} \tag{7}$$

where θ_i denotes the azimuthal angle of the ith scatterer, $f_i(m, t')$ denotes the instantaneous frequency obtained from (6), and d denotes the distance between the neighbouring elements, respectively. In this paper, the targets are located in the far-field and the observation time in one CPI is very short, thus the angles of the target are assumed to be constant during one CPI. It is seen in (7) that the phase delay is not only related to the element index l, but also to the fast-time t'. Given that the phase delay between elements is a function of frequency for wideband DOA and the instantaneous frequency is the function of fast-time for the FMCW signal, $\varphi_i^{(l)}$ can be transferred to a function of fast-time t'. Moreover, the phase delay between elements is decomposed into the narrowband component $2\pi f_0 \frac{ld}{c}\sin\theta_i$ related to the starting frequency and an additional term $2\pi\mu t' \frac{ld}{c}\sin\theta_i$, which is coupled between the antenna indices l and the fast-time t'. This wideband DOA problem in estimating joint parameters has been ignored in many articles [7], [34], [35]. The general wideband DOA solutions of CSSM or ISSM, which analyse the DOA information for each sub-band signal after Fourier transform, are avoided by addressing the coupling terms.

The received signal is then mixed with the conjugate copy of the transmitted signal (called the de-chirping process), and the de-chirped signal (also called beat frequency signal) of the ith scatterer received by the lth element can be written as [4]

$$\begin{aligned} y_i^{(l)}(m, t') &= r_i^{(l)}(m, t')s^*(m, t') \\ &\approx \alpha_i' \exp\left[j2\pi(f_0 + \mu t')\frac{ld}{c}\sin\theta_i\right] \\ &\quad \times \exp\left[-j2\pi\left(f_0\frac{2v_i}{c}T_r m + \mu\gamma_i t'\right)\right] \\ &\quad \times \exp\left[-j2\pi\mu\frac{2v_i}{c}T_r m t'\right], \\ &\text{with } t' \in [\Gamma, T_0], \end{aligned} \tag{8}$$

where Γ is the round trip time of the maximum unambiguous range and α_i' is the constant complex amplitude (for simplicity, α_i is still used in the following). When sampling the data with respect to fast-time with sampling frequency f_s, the discretised data $\mathrm{y}_i^{(l)}$ are obtained as

$$\begin{aligned} \mathrm{y}_i^{(l)}(m, k) &= \alpha_i \exp[j2\pi(a(\theta_i)l + f_d(v_i)m + f_r(R_i)k)] \\ &\quad \times \exp[j2\pi(f_{\theta r}(\theta_i)lk + f_{dr}(v_i)mk)], \end{aligned} \tag{9}$$

where $k = \frac{t'}{f_s}$ represents the indices of fast-time samples ($k = 0, 1, 2 \ldots, K-1$ and K is the total number of samples in one PRI), and the notations $a(\theta_i) = f_0 \frac{d}{c} \sin\theta_i$, $f_d(v_i) = -f_0 \frac{2v_i}{c} T_r$, $f_r(R_i) = -\frac{\mu}{f_s}\gamma_i$, $f_{\theta r}(\theta_i) = \mu \frac{d}{cf_s} \sin\theta_i$ and $f_{dr}(v_i) = -\mu \frac{2v_i}{cf_s} T_r$ are used to simplify the equation.

For the following analysis and algorithm development, the data are represented compactly. Before illustrating the signal model, we first define the notations of the DOA steering vector $\mathbf{a}(\theta_i) \in \mathbb{C}^{L\times 1}$, slow-time sinusoidal vector $\mathbf{f}_d(v_i) \in \mathbb{C}^{M\times 1}$, fast-time sinusoidal vector $\mathbf{f}_r(R_i) \in \mathbb{C}^{K\times 1}$, the matrices of wideband DOA coupling $\mathbf{\Psi}(\theta_i) \in \mathbb{C}^{L\times K}$ and range migration coupling $\mathbf{\Phi}(v_i) \in \mathbb{C}^{M\times K}$, respectively, as

$$\begin{aligned} \mathbf{a}(\theta_i) &= [1, e^{j2\pi a(\theta_i)}, \ldots, e^{j2\pi a(\theta_i)(L-1)}]^T, \\ \mathbf{f}_d(v_i) &= [1, e^{j2\pi f_d(v_i)}, \ldots, e^{j2\pi f_d(v_i)(M-1)}]^T, \\ \mathbf{f}_r(R_i) &= [1, e^{j2\pi f_r(R_i)}, \ldots, e^{j2\pi f_r(R_i)(K-1)}]^T, \\ \mathbf{\Psi}(\theta_i) &= \begin{pmatrix} \mathbf{h}_0^T(\theta_i) \\ \mathbf{h}_1^T(\theta_i) \\ \vdots \\ \mathbf{h}_{L-1}^T(\theta_i) \end{pmatrix}, \quad \mathbf{\Phi}(v_i) = \begin{pmatrix} \mathbf{g}_0^T(v_i) \\ \mathbf{g}_1^T(v_i) \\ \vdots \\ \mathbf{g}_{M-1}^T(v_i) \end{pmatrix}, \end{aligned} \tag{10}$$

with $\mathbf{h}_l(\theta_i) \in \mathbb{C}^{K\times 1}$ and $\mathbf{g}_m(v_i) \in \mathbb{C}^{K\times 1}$ defined as

$$\begin{aligned} \mathbf{h}_l(\theta_i) &= [1, e^{j2\pi l f_{\theta r}(\theta_i)}, \ldots, e^{j2\pi l f_{\theta r}(\theta_i)(K-1)}]^T, \\ \mathbf{g}_m(v_i) &= [1, e^{j2\pi m f_{dr}(v_i)}, \ldots, e^{j2\pi m f_{dr}(v_i)(K-1)}]^T. \end{aligned} \tag{11}$$

Let $[\boldsymbol{\mathcal{P}}(\theta_i)]_{l,0,k} = [\mathbf{\Psi}(\theta_i)]_{l,k}$, which means adding a new axis between the row and the column of $\mathbf{\Psi}(\theta_i)$ to make it a three-dimensional tensor $\boldsymbol{\mathcal{P}}(\theta_i) \in \mathbb{C}^{L\times 1\times K}$. Then, the wideband DOA coupling tensor $\boldsymbol{\mathcal{W}}_{\theta r}(\theta_i) \in \mathbb{C}^{L\times M\times K}$ and the range migration coupling tensor $\boldsymbol{\mathcal{W}}_{dr}(v_i) \in \mathbb{C}^{L\times M\times K}$ of ith target, respectively, are defined as

$$\begin{aligned} \boldsymbol{\mathcal{W}}_{\theta r}(\theta_i) &= \boldsymbol{\mathcal{P}}(\theta_i) \times_2 \mathbf{1}_M, \\ \boldsymbol{\mathcal{W}}_{dr}(v_i) &= \mathbf{1}_L \circ \mathbf{\Phi}(v_i). \end{aligned} \tag{12}$$

Accordingly, the three-dimensional tensor $\boldsymbol{\mathcal{Y}} \in \mathbb{C}^{L\times M\times K}$ for multiple targets in the presence of white Gaussian noise is written as

$$\begin{aligned} \boldsymbol{\mathcal{Y}} = \sum_{i=1}^{I} \alpha_i \mathbf{a}(\theta_i) \circ \mathbf{f}_d(v_i) \circ \mathbf{f}_r(R_i) \odot \boldsymbol{\mathcal{W}}_{\theta r}(\theta_i) \odot \boldsymbol{\mathcal{W}}_{dr}(v_i) \\ + \boldsymbol{\mathcal{N}}, \end{aligned} \tag{13}$$

where $\boldsymbol{\mathcal{N}} \in \mathbb{C}^{L\times M\times K}$ is the complex Gaussian noise tensor with entries' distribution $\mathcal{CN}(0, \sigma^2)$.

Now the problem is to estimate the parameters θ_i, v_i and R_i for all I point targets from the tensor data $\boldsymbol{\mathcal{Y}}$, where the cubic data $\boldsymbol{\mathcal{Y}}$ are indexed with the array element indices $l = 0, 1, \ldots, L-1$, slow-time indices $m = 0, 1, \ldots, M-1$ and fast-time sampling indices $k = 0, 1, \ldots, K-1$.

Compared to the narrowband signal model, in which the coupling terms $\boldsymbol{\mathcal{W}}_{\theta r}(\theta_i)$ and $\boldsymbol{\mathcal{W}}_{dr}(v_i)$ are negligible, the maximum absolute influence in fast-time will be $f_{dr}(v_i)(M-1) \approx -\frac{v_i \mathrm{CPI}}{\Delta r} \frac{1}{K}$, where $\Delta r = \frac{c}{2B}$ is the theoretical range resolution, which means one can see observable degradation in the spectrum when the target moves more than one range cell resolution within one CPI. Similarly, the DOA the maximum influence of $\frac{f_{\theta r}(\theta_i)(K-1)}{a(\theta_i)} \approx \frac{B}{f_0}$ $(\theta_i \neq 0)$ equals to the relative bandwidth. Thus, the DOA degradation depends on both the relative bandwidth and angle θ_i. Although ignoring the coupling term $\boldsymbol{\mathcal{W}}_{\theta r}(\theta_i)$ in the signal model might not result in large errors in the DOA estimation, the Doppler ambiguity information hidden in the $\boldsymbol{\mathcal{W}}_{dr}(v_i)$ can no longer be resolved.

B. Ambiguous Doppler Velocity

According to (9) and the Nyquist criterion, the maximum unambiguous angle $\theta_{\max}$, Doppler velocity $v_{\max}$ and range $R_{\max}$ are determined by $a(\theta_i) \in [-0.5, 0.5)$, $f_d(v_i) \in [-0.5, 0.5)$ and $f_r(R_i) \in [0, 1)$ as follows

$$\begin{aligned} \sin(\theta_{\max}) &= \min\left\{\frac{c}{2f_0 d}, 1\right\}, \\ v_{\max} &= \frac{c}{4T_r f_0}, \\ R_{\max} &= \frac{cK}{2B} = K\Delta r. \end{aligned} \tag{14}$$

Here we assume that the azimuthal angles of the targets are within the unambiguous domain, and it is usually realised by setting the distance of neighbouring antenna as $d = \frac{c}{2f_0}$ to cover the whole azimuthal domain unambiguously. If the Doppler velocity v_i is larger than the maximum unambiguous velocity $v_{\max}$, it will be folded into the unambiguous domain of the sinusoidal components $f_d(v_i)$ according to

$$v_i = 2n_i v_{\max} + \bar{v}_i, \tag{15}$$

where $|\bar{v}_i| < |v_{\max}|$ is the folded velocity and n_i is the integer fold number. Estimating the velocity from $f_d(v_i) = f_d(\bar{v}_i)$ would only yield the folded velocity $\bar{v}_i$, while the information regarding the Doppler ambiguity can be extracted from the coupling component $f_{dr}(v_i)$. Here we assume that the $|f_{dr}(v_i)| < 0.5$ to avoid coupling term ambiguity, and it is usually satisfied in most applications when $|v_i| < \frac{cf_s}{4B}$ holds.

According to (14), the constraint between $v_{\max} R_{\max}$ and the sampling frequency f_s has

$$v_{\max} R_{\max} \leq \frac{c^2}{8Bf_0} f_s, \tag{16}$$

where $\frac{c^2}{8Bf_0}$ is a constant determined by the radar system. For a given system, $v_{\max} R_{\max}$ is bounded by the sampling frequency f_s. It is indicated in (16) that for UWB FMCW radar, large $v_{\max}$ and $R_{\max}$ are usually difficult to achieve simultaneously using the low-cost hardware (low sampling frequency). Such a constraint limits the application of UWB FMCW radar in many industrial fields. For example, to simultaneously achieve $v_{\max} = 100$ m/s and $R_{\max} = 200$ m for 77 GHz automotive radar with 4 GHz bandwidth, a sampling frequency of at least 500 MHz is required. Moreover, a higher sampling frequency implies a larger amount of data to be collected and processed in a limited time interval, which is computationally heavy as well as memory-consuming. A possible way to alleviate the burden on the hardware is to relax the maximum unambiguous velocity $v_{\max}$ and recover the true ambiguous velocity $|v_i| > |v_{\max}|$ from the coupling term

$f_{dr}(v_i)$, which is one of the main objectives of this paper. A novel spectral norm-based algorithm is proposed to address this problem in the next section.

III. Single Target

The joint estimation of range $\mathbf{r}$, velocity $\mathbf{v}$ and DOA $\boldsymbol{\theta}$ from the signal model (13) is a highly non-linear problem. In this section, we consider a single point target and propose a novel spectral-norm based algorithm for target parameter estimation. Then, a new alternative update method is introduced to ensure the estimation accuracy.

Assume that there is only the ith target presented and all the interferences from other targets are removed or negligible. The data are presented as

$$\boldsymbol{\mathcal{Y}}_i = \alpha_i \mathbf{a}(\theta_i) \circ \mathbf{f}_d(v_i) \circ \mathbf{f}_r(R_i) \odot \boldsymbol{\mathcal{W}}_{\theta r}(\theta_i) \odot \boldsymbol{\mathcal{W}}_{dr}(v_i) + \boldsymbol{\mathcal{N}}. \tag{17}$$

Since the coupling terms are the functions of the ambiguous velocity v_i and the DOA θ_i, the proposed method attempts to estimate these parameters from the coupling terms first.

A. Coupling Terms Estimation

In this subsection, we first describe the traditional coherent integration method for estimating parameters from the coupling terms and the drawbacks of this method are discussed. Second, we introduce a novel spectral norm-based method which performs better than conventional coherent integration approaches, especially when the data size is limited.

- Coherent integration-based method

Conventional integration-based methods are developed with a matched filter bank and usually can be implemented via multi-dimensional fast Fourier transform (FFT) if the data are uniformly sampled. For the signal model (17), this method can be written as

$$\check{v}_i, \check{\theta}_i = \underset{v,\theta}{\operatorname{argmax}} \, ||\mathscr{F}[\boldsymbol{\mathcal{Y}}_i \odot \boldsymbol{\mathcal{W}}^*_{\theta r}(\theta) \odot \boldsymbol{\mathcal{W}}^*_{dr}(v)]||_{\max}, \tag{18}$$

where the checkmark $\check{(\cdot)}$ denotes the parameters estimated from the coupling terms. $\check{v}_i$ is the unambiguous velocity, which can be much larger than $v_{\max}$ or smaller than $-v_{\max}$. Estimates are based on peak detection of the coherently integrated energy of the compensated signals. If the coupling terms are correctly compensated, meaning that the ith target is focused, the integrated energy of the target will produce a maximum. The form of (18) corresponds to the Generalised RFT proposed in [24] if the array element dimension is removed, meaning that (18) is the 3-dimensional form of RFT. Although various coherent integration algorithms are mentioned in Section I, (18) is sufficient to be used as the benchmark hereinafter since the optimality of RFT is demonstrated to perform coherent integration for rectilinearly moving targets under a white Gaussian noise background in [25].

Since the Fourier spectrum is grid-based and can only yield an on-grid peak, even if the coupling terms are correctly compensated the maximum spectrum might miss the Fourier grids. In such cases, the on-grid peak of the Fourier spectrum may return a highly inaccurate estimation of $\check{v}_i$ and result in incorrect fold number extraction. The off-grid problem regarding Doppler ambiguity estimation is severe when the neighbouring slow-time frequency grids return different fold number estimations, which means

$$|f_{dr}(v_i) - f_{dr}(v_i + 2v_{\max})|(K-1) < \frac{1}{M}. \tag{19}$$

After reorganising the inequality, we get the condition

$$M < \frac{f_0}{B}, \tag{20}$$

and we conclude that the problem of resolving the off-grid Doppler ambiguity is severe when (20) is satisfied even under conditions of very high SNR. Thus, when data size is moderate, dense zero-padding is needed to create the over-complete Fourier basis to match the data, which is both time- and memory-consuming. This problem will be explained in detail in Section VI.

- Norm-based method

To address the off-grid problem, we propose a novel spectral norm-based method which can estimate the location of an off-grid peak. To show the proposed algorithm, the data model $\boldsymbol{\mathcal{Y}}_i$ is reshaped into the matrix form $\mathbf{Y}_i \in \mathbb{C}^{LM \times K}$ by stacking the array element and slow-time dimensions together as

$$\mathbf{Y}_i = \begin{pmatrix} [\boldsymbol{\mathcal{Y}}_i]_{0,:,:} \\ [\boldsymbol{\mathcal{Y}}_i]_{1,:,:} \\ \vdots \\ [\boldsymbol{\mathcal{Y}}_i]_{L-1,:,:} \end{pmatrix}. \tag{21}$$

Rewriting the $\mathbf{Y}_i$ compactly as

$$\mathbf{Y}_i = \alpha_i [\mathbf{a}(\theta_i) \otimes \mathbf{f}_d(v_i)] \mathbf{f}_r^T(R_i) \odot \boldsymbol{\Omega}_{\theta r}(\theta_i) \odot \boldsymbol{\Omega}_{dr}(v_i) + \mathbf{N}, \tag{22}$$

where $\mathbf{N} \in \mathbb{C}^{ML \times K}$ is the complex discrete noise, $\boldsymbol{\Omega}_{\theta r}(\theta_i) \in \mathbb{C}^{LM \times K}$ and $\boldsymbol{\Omega}_{dr}(v_i) \in \mathbb{C}^{LM \times K}$ are

$$\begin{aligned} \boldsymbol{\Omega}_{\theta r}(\theta_i) &= \boldsymbol{\Psi}(\theta_i) \otimes \mathbf{1}_M, \\ \boldsymbol{\Omega}_{dr}(v_i) &= \mathbf{1}_L \otimes \boldsymbol{\Phi}(v_i). \end{aligned} \tag{23}$$

Letting $\mathbf{X}_i = \alpha_i [\mathbf{a}(\theta_i) \otimes \mathbf{f}_d(v_i)] \mathbf{f}_r^T(R_i)$, which is a rank-one matrix, we can show the inequality

$$||\mathbf{X}_i \odot \boldsymbol{\Omega}_{\theta r}(\theta_i) \odot \boldsymbol{\Omega}_{dr}(v_i)||_2 \leq ||\mathbf{X}_i||_2, \tag{24}$$

with the following proof

Proof: Because

$$\begin{aligned} &||\mathbf{X}_i \odot \boldsymbol{\Omega}_{\theta r}(\theta_i) \odot \boldsymbol{\Omega}_{dr}(v_i)||_2 \\ &\quad \leq ||\mathbf{X}_i \odot \boldsymbol{\Omega}_{\theta r}(\theta_i) \odot \boldsymbol{\Omega}_{dr}(v_i)||_F \\ &\quad = \sqrt{\sum\nolimits_p \sum\nolimits_q |[\mathbf{X}_i]_{p,q}|^2 \cdot |[\boldsymbol{\Omega}_{\theta r}(\theta_i)]_{p,q}|^2 \cdot |[\boldsymbol{\Omega}_{dr}(v_i)]_{p,q}|^2} \\ &\quad = \sqrt{\sum\nolimits_p \sum\nolimits_q |[\mathbf{X}_i]_{p,q}|^2} \\ &\quad = ||\mathbf{X}_i||_F \\ &\quad = ||\mathbf{X}_i||_2, \end{aligned} \tag{25}$$

where $|[\boldsymbol{\Omega}_{\theta r}(\theta_i)]_{p,q}|^2 = |[\boldsymbol{\Omega}_{dr}(v_i)]_{p,q}|^2 = 1$ and the equality holds iff. $\mathbf{X}_i \odot \boldsymbol{\Omega}_{\theta r}(\theta_i) \odot \boldsymbol{\Omega}_{dr}(v_i)$ is a rank-one matrix, which obviously is not (since it cannot be formulated by matrix product

of two vectors). Here the property $||\mathbf{X}||_2 \leq ||\mathbf{X}||_F$ (equality holds iff. $\mathbf{X}$ is a rank-one matrix or a zero matrix) is used [36].

According to the inequality (24), the parameters in the coupling terms can be extracted as

$$\begin{aligned}\check{v}_i, \check{\theta}_i &= \underset{v,\theta}{\operatorname{argmax}} ||\mathbf{Y}_i \odot \mathbf{\Omega}^*_{\theta r}(\theta) \odot \mathbf{\Omega}^*_{dr}(v)||_2 \\ &= \underset{v,\theta}{\operatorname{argmax}} ||\mathbf{X}_i \odot \mathbf{\Omega}_{\theta r}(\theta_i - \theta) \odot \mathbf{\Omega}_{dr}(v_i - v) \\ &\qquad + \mathbf{N} \odot \mathbf{\Omega}^*_{\theta r}(\theta) \odot \mathbf{\Omega}^*_{dr}(v)||_2 \\ &\approx \underset{v,\theta}{\operatorname{argmax}} ||\mathbf{X}_i \odot \mathbf{\Omega}_{\theta r}(\theta_i - \theta) \odot \mathbf{\Omega}_{dr}(v_i - v)||_2. \quad (26)\end{aligned}$$

We assume the presence of white Gaussian noise and that the noise energy is uniformly distributed across the entire data set and uncorrelated with the signal. Moreover, the compensation terms only change the phase of the noise and will not affect the SNR. Therefore, the noise term can be omitted and exact expression is replaced by the approximation valid for high SNR values.

It is worth noting that the matrix stacking in (21) is important when performing matrix manipulation for multi-way data [4]. According to the simulation results, tensor decomposition (TD) [33] could provide similar performance. However, it has not yet been proven mathematically, and TD is computationally heavier than the matrix norm computation.

The non-linear optimisation of (26) requires a two-dimensionally exhaustive search on the ambiguous velocity v and angle θ simultaneously. In Section V we demonstrate that (26) can be decomposed into two separate one-dimensional searches via the data reshaping.

Unlike with the integration-based method, the peak is found without the use of Fourier grids. Thus, the problem of off-grid estimates from the coupling terms can be avoided. A detailed comparison will be presented in Section VI.

B. Frequencies Estimation

A separate analysis of the CRBs of the folded velocity $\hat{v}_i$ from the sinusoids and the unambiguous velocity $\check{v}_i$ from the coupling term (see Appendix B) shows the estimation accuracy of $\hat{v}_i$ to be much higher than that of $\check{v}_i$. Thus, the parameter estimations from the coupling terms are less reliable and less accurate than those from the sinusoids. However, more accurate parameters (azimuth, folded velocity and range) can be obtained from the sinusoids after compensation of the coupling terms using coarse estimations (azimuth $\check{\theta}_i$ and unambiguous velocity $\check{v}_i$). With the coarse estimates $\check{v}_i$ and $\check{\theta}_i$ from (26), the compensation terms are formulated as $\boldsymbol{\mathcal{W}}^*_{dr}(\check{v}_i)$ and $\boldsymbol{\mathcal{W}}^*_{\theta r}(\check{\theta}_i)$. If performed with $\boldsymbol{\mathcal{Y}}_i \odot \boldsymbol{\mathcal{W}}^*_{\theta r}(\check{\theta}_i) \odot \boldsymbol{\mathcal{W}}^*_{dr}(\check{v}_i)$, the new decoupled data are obtained. Since there is only one target presented, and for the purpose of simplicity, the method for parameter estimation is given from the decoupled data using matched filter

$$\begin{aligned}\tilde{\boldsymbol{\mathcal{Y}}}_i &= \boldsymbol{\mathcal{Y}}_i \odot \boldsymbol{\mathcal{W}}^*_{\theta r}(\check{\theta}_i) \odot \boldsymbol{\mathcal{W}}^*_{dr}(\check{v}_i), \\ \hat{v}_i, \tilde{\theta}_i, \tilde{R}_i &= \underset{v,\theta,R}{\operatorname{argmax}} ||\tilde{\boldsymbol{\mathcal{Y}}}_i \times_1 \mathbf{a}(\theta) \times_2 \mathbf{f}_d(v) \times_3 \mathbf{f}_r(R)||_{\max}, \end{aligned} \quad (27)$$

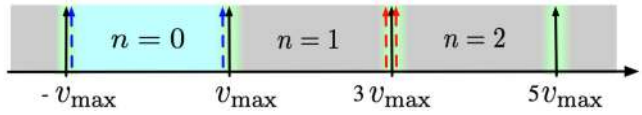

Fig. 1. Illustration of fold number estimation.

where $\tilde{(\cdot)}$ denotes the estimated parameter.

C. Fold Number Estimation

Once the coarse unambiguous velocity $\check{v}_i$ and the folded velocity $\hat{v}_i$ are estimated, the initial fold number estimation can be obtained according to (15) as

$$\tilde{n}_i = \left\lfloor \frac{\check{v}_i + v_{\max}}{2v_{\max}} \right\rfloor, \quad (28)$$

and a more accurate estimation of the unambiguous velocity is given as

$$\tilde{v}_i = \hat{v}_i + 2v_{\max}\tilde{n}_i. \quad (29)$$

It is shown in (29) that the unambiguous velocity is divided into the folded velocity $\hat{v}_i$ (estimated from sinusoidal components) and the fold number (extracted from the coupling components).

This works very well in most cases. However, (29) fails in the worst case when the velocity v_i is very close to $(2n+1)v_{\max}$. The problem is illustrated in Fig. 1, where (29) works when the targets are located in the grey or cyan regions. However, if the target is located close to $(2n+1)v_{\max}$ (green region in Fig. 1), for instance when assuming $v_i = 3v_{\max}$, the estimate from the coupling component returns $\check{v}_i \approx 3v_{\max}$ (indicated as red dashed arrows), then (29) could return an uncertain fold number of 1 or 2 depending on the noise, interference from the other targets and the computational accuracy. Additionally, the estimate $\hat{v}_i$ from the sinusoidal component is $|\hat{v}_i| \approx v_{\max}$ (indicated as blue dashed arrows), which could return $\hat{v}_i \lesssim v_{\max}$ or $\hat{v}_i \gtrsim -v_{\max}$. Therefore, there are four possible combinations of (29), and for each one a different $\tilde{v}_i$ would be obtained. This problem would happen in each iteration of the RELAX algorithm and would influence the convergence of RELAX algorithm significantly.

To solve this problem, a novel approach is introduced. Since if $v_i \approx (2n+1)v_{\max}$, we have $|\hat{v}_i| \approx v_{\max}$, a threshold ε is set to test the difference $||\hat{v}_i| - v_{\max}|$, and this threshold is determined by the accuracy of the estimate $\hat{v}_i$ (which can be determined by CRB). If $||\hat{v}_i| - v_{\max}| \leq \varepsilon$ is satisfied, (28) is modified by replacing floor operation $\lfloor\rfloor$ by round operation $\lfloor\rceil$ to obtain the uncertain fold number. The fold number can then be determined according to the sign of $\hat{v}_i$. If $\hat{v}_i < 0$, the fold number can be estimated with more confidence; otherwise, the fold number is probably overestimated.

According to the analysis, the fold number estimation is summarised in Algorithm 1(**A**1).

D. Refine the Parameters by Alternation

As mentioned earlier, the unambiguous velocity estimate $\check{v}_i$ is coarse and inaccurate, which may result in inaccurate estimations of $\hat{v}_i$ and $\tilde{n}_i$. Thus, a novel refinement method is introduced to improve the accuracy of these estimations by alternatively

Algorithm 1: Fold Number Estimation Algorithm (**A**1).

Input: $\hat{v}_i$, $\check{v}_i$, $v_{\max}$, ε
if $||\hat{v}_i| - v_m| > \varepsilon$:
  $\tilde{n}_i \Leftarrow \lfloor \frac{\check{v}_i + v_{\max}}{2v_{\max}} \rfloor$
  $\tilde{v}_i \Leftarrow \hat{v}_i + 2v_{\max}\tilde{n}_i$
else:
  $\tilde{n}_i \Leftarrow \lfloor \frac{\check{v}_i + v_{\max}}{2v_{\max}} \rceil$
  if $\hat{v}_i > 0$:
    $\tilde{n}_i \Leftarrow \tilde{n}_i - 1$
  endif:
  $\tilde{v}_i \Leftarrow \hat{v}_i + 2v_{\max}\tilde{n}_i$
endif
Output: $\tilde{n}_i$, $\tilde{v}_i$

updating $\tilde{v}_i, \tilde{\theta}_i$ by (27) and (29) and updating $\boldsymbol{\mathcal{W}}^*_{dr}(\check{v}_i), \boldsymbol{\mathcal{W}}^*_{\theta r}(\check{\theta}_i)$ by $\check{v}_i,\ \check{\theta}_i \Leftarrow \tilde{v}_i,\ \tilde{\theta}_i$. The reason is straightforward: having accurate $\tilde{v}_i$ and $\tilde{\theta}_i$ leads to accurate coupling terms compensation, which in return increases the accuracy of $\tilde{v}_i$ and of $\tilde{\theta}_i$. Since the alternative method converges very quickly, only 3 or 4 repeats are sufficient for convergence. Although the alternation process only needs a few repeats, it is essential and influences the estimation results significantly. A comparison of with and without such alternation will be shown in Section VI.

E. Amplitude Estimation

As we have already estimated the frequencies, the estimation of the complex amplitude is directly given as

$$\tilde{\alpha}_i = \frac{1}{LMK}[\boldsymbol{\mathcal{Y}}_i \odot \boldsymbol{\mathcal{W}}^*_{\theta r}(\check{\theta}_i) \odot \boldsymbol{\mathcal{W}}^*_{dr}(\check{v}_i)] \times_1 \mathbf{a}(\tilde{\theta}_i) \times_2 \mathbf{f}_d(\hat{v}_i) \times_3 \mathbf{f}_r(\tilde{R}_i). \tag{30}$$

Although the alternation of steps can optimise the solutions, (27) is still an on-grid estimation. As soon as a relatively accurate estimation is obtained as an initial result, the Nelder-Mead method [37] is adopted to optimise the estimation of the local optimal off-grid solution as

$$\tilde{\boldsymbol{\mathcal{Y}}}_i = \boldsymbol{\mathcal{Y}}_i \odot \boldsymbol{\mathcal{W}}^*_{\theta r}(\check{\theta}_i) \odot \boldsymbol{\mathcal{W}}^*_{dr}(\check{v}_i),$$
$$\tilde{\alpha}_i, \tilde{v}_i, \tilde{\theta}_i, \tilde{R}_i = \underset{\alpha, v, \theta, R}{\operatorname{argmax}} ||\tilde{\boldsymbol{\mathcal{Y}}}_i - \alpha \mathbf{a}(\theta) \circ \mathbf{f}_d(v) \circ \mathbf{f}_r(R)||_F. \tag{31}$$

The algorithm for a single target is summarised as Algorithm 2 (**A**2).

IV. Multiple Targets

In this section, the multiple target scenario is considered and the estimation is performed. In cases where there are multiple targets, the greedy and RELAX algorithms are adopted and modified to help to reduce the multi-target problem to a sequence of single target problems, for which (24) is proven. Both the greedy algorithm and the RELAX algorithm have been widely used and show the effective performance in many applications [5], [7], [38]–[43]. Thus, the general ideas of the greedy and RELAX algorithms are adapted to the multiple-target scenario with the proposed method of the single target.

Algorithm 2: Alternation Algorithm (**A**2).

Estimate
  $\check{v}_i, \check{\theta}_i \Leftarrow \underset{v,\theta}{\operatorname{argmax}} ||\mathbf{Y}_i \odot \boldsymbol{\Omega}^*_{\theta r}(\theta) \odot \boldsymbol{\Omega}^*_{dr}(v)||_2$
repeat
  Update $\hat{v}_i, \tilde{\theta}_i, \tilde{R}_i$ from (27)
  Update $\tilde{v}_i$ according to **A**1
  Update $\check{v}_i,\ \check{\theta}_i \Leftarrow \tilde{v}_i,\ \tilde{\theta}_i$
  Update $\boldsymbol{\mathcal{W}}^*_{dr}(\check{v}_i)$ and $\boldsymbol{\mathcal{W}}^*_{\theta r}(\check{\theta}_i)$
until the stop criteria satisfied
Estimate $\tilde{\alpha}_i$ from (30)
Optimise (31) using Nelder-Mead method
Output: $\tilde{\alpha}_i,\ \tilde{v}_i,\ \tilde{\theta}_i,\ \tilde{R}_i$

Algorithm 3: Greedy Algorithm (**A**3).

$\boldsymbol{\mathcal{Z}} \Leftarrow \boldsymbol{\mathcal{Y}}$, $i \Leftarrow 0$
repeat
  $i \Leftarrow i + 1$
  Estimate ith parameters $\tilde{\boldsymbol{\vartheta}}_i$ using **A**2 from $\boldsymbol{\mathcal{Z}}$
  Formulate $\tilde{\boldsymbol{\mathcal{Z}}}_i$, and remove it from $\boldsymbol{\mathcal{Z}}$ as (32)
until $|\tilde{\alpha}_i| \leq \epsilon_1$
Output: number of targets $\tilde{I} \Leftarrow i$ and all the corresponding features $\tilde{\boldsymbol{\vartheta}}_i = [\tilde{\alpha}_i,\ \tilde{v}_i,\ \tilde{\theta}_i,\ \tilde{R}_i]$

A. Greedy Algorithm

For multiple targets, the greedy algorithm is performed to extract and remove each target sequentially. By applying **A**2 to the raw data, the parameters of the target with maximum magnitude will be estimated. Construct the reflected signal as $\tilde{\boldsymbol{\mathcal{Z}}}_i$ and subtract it from the data as

$$\tilde{\boldsymbol{\mathcal{Z}}}_i \Leftarrow \tilde{\alpha}_i \mathbf{a}(\tilde{\theta}_i) \circ \mathbf{f}_d(\tilde{v}_i) \circ \mathbf{f}_r(\tilde{R}_i) \odot \boldsymbol{\mathcal{W}}_{\theta r}(\tilde{\theta}_i) \odot \boldsymbol{\mathcal{W}}_{dr}(\tilde{v}_i),$$
$$\boldsymbol{\mathcal{Z}} \Leftarrow \boldsymbol{\mathcal{Z}} - \tilde{\boldsymbol{\mathcal{Z}}}_i, \tag{32}$$

where the initialisation is made with $\boldsymbol{\mathcal{Z}} \Leftarrow \boldsymbol{\mathcal{Y}}$. Repeat **A**2 by updating $\boldsymbol{\mathcal{Z}}$ in (32) until some stopping condition is satisfied. Here a threshold of magnitude is selected as the criterion for the stopping condition and to define the number of targets for simplicity. The greedy algorithm stops if the magnitude of the ith target is smaller than the threshold ϵ_1. The selected threshold ϵ_1 can be relatively smaller, and the number of targets is allowed to be slightly overestimated since it will be reconsidered later.

This algorithm is summarised as Algorithm 3 (**A**3).

B. RELAX Method

The estimation results of **A**3 are coarse because the mutual interference between the targets affects the estimation of other targets and the estimation error accumulates with the increase of the number of targets in the scene. To address this problem, an iterative parameter estimation method is presented in this subsection [38].

If we assume the number of the targets has been estimated, which can be incorrect and will be reconsidered in the following, the parameters of the ith targets can be re-estimated by **A**2 from

Algorithm 4: RELAX Algorithm (**A**4).

1: Apply **A**3 for initial parameters estimation
2: **repeat**
3: $\boldsymbol{\mathcal{Z}} \Leftarrow \boldsymbol{\mathcal{Y}}$
4: **for** $i = 1 : \tilde{I}$ **do**
5: $\boldsymbol{\mathcal{Z}}_i \Leftarrow \boldsymbol{\mathcal{Z}} - \sum_{p \neq i} \tilde{\boldsymbol{\mathcal{Z}}}_p$
6: Estimate ith parameters using **A**2 from $\boldsymbol{\mathcal{Z}}_i$ and reformulate $\tilde{\boldsymbol{\mathcal{Z}}}_i$, where (26) is replaced by (34) and (28) is replaced by (35)
7: **end for**
8: After several iterations, abandon the targets according to $|\tilde{\alpha}_i| \leq \epsilon_2$ and update $\tilde{I}$
9: **until** some stop criteria satisfied

the data without interference from the other targets

$$\boldsymbol{\mathcal{Z}}_i \Leftarrow \boldsymbol{\mathcal{Y}} - \sum_{p \neq i} \tilde{\boldsymbol{\mathcal{Z}}}_p. \tag{33}$$

Thus, the new parameters are estimated without interference from the side lobes or spread spectrum from the other targets. This algorithm loops from $i = 1$ to $i = \tilde{I}$. For a more accurate estimation, it would need to be repeated multiple times. As the number of targets may be slightly overestimated, a more demanding threshold ϵ_2 can be set after several iterations. Once the magnitude is lower than ϵ_2 in the iteration, the corresponding target is abandoned.

To save the computational time, (26) is replaced with

$$\check{n}_i, \check{\theta}_i = \underset{n,\theta}{\operatorname{argmax}} ||\mathbf{Y} \odot \boldsymbol{\Omega}^*_{\theta r}(\theta) \odot \boldsymbol{\Omega}^*_{dr}(\hat{v}_i + 2n v_{\max})||_2, \tag{34}$$

and (28) in **A**2 is replaced by

$$\tilde{n}_i \Leftarrow \check{n}_i. \tag{35}$$

Because we already have a relatively accurate estimation of the folded velocity $\hat{v}_i$, the information desired from the coupling term is the fold number $\tilde{n}_i$. The stopping criterion can be made based on the estimation convergence. We note that rewriting the objective function (26) as (34), the fold number can be determined via the objective function directly. Then (26) and (34) are actually identical, where (26) searches on unfolded velocity and (34) needs to search on folded velocity and the fold number simultaneously. However, the fold number using (34) is yet highly inaccurate, so **A**1 has to be applied or embedded to increase the estimation accuracy of fold number in (34).

The iterative algorithm is summarised in Algorithm4 (**A**4).

Estimating the number of scatterers is usually a difficult problem, especially in the presence of the coupling components. Although the proposed magnitude thresholding works very well when the targets are far apart from each other, it may be difficult to define the thresholds when there are too many closely spaced targets within the Rayleigh resolution. An alternative way to do this is to combine the proposed method with the generalised Akaike information criterion (GAIC). Since this is not the main contribution of this paper, readers are referred to [5] for details.

V. Efficient Implementation

It is time-consuming to solve (26) with a simultaneous two-dimensional search. In this section, we introduce a novel method to solve it efficiently. In fact, (26) can be solved separately by two one-dimensional searches on v and θ. Below, the method for estimating $\check{v}_i$ is shown as an example. To do this, we reshape the tensor data (17) to a new matrix form by stacking the array element and the fast-time dimensions together in matrix $\mathbf{V}_i \in \mathbb{C}^{M \times LK}$ as

$$\mathbf{V}_i = \left([\boldsymbol{\mathcal{Y}}_i]_{0,:,:}, [\boldsymbol{\mathcal{Y}}_i]_{1,:,:}, \cdots [\boldsymbol{\mathcal{Y}}_i]_{L-1,:,:}\right). \tag{36}$$

This can be written compactly as

$$\begin{aligned}\mathbf{V}_i &= \alpha_i \mathbf{f}_d(v_i)[\mathbf{a}(\theta_i) \otimes \mathbf{f}_r(R_i)]^T \\ &\quad \odot \left[\mathbf{1}_M \boldsymbol{\psi}^T(\theta_i)\right] \odot \left[\mathbf{1}_L^T \otimes \boldsymbol{\Phi}(v_i)\right] + \bar{\mathbf{N}} \\ &= \alpha_i \mathbf{f}_d(v_i) \left[\mathbf{a}(\theta_i) \otimes \mathbf{f}_r(R_i) \odot \boldsymbol{\psi}(\theta_i)\right]^T \\ &\quad \odot \left[\mathbf{1}_L^T \otimes \boldsymbol{\Phi}(v_i)\right] + \bar{\mathbf{N}},\end{aligned} \tag{37}$$

where $\boldsymbol{\psi}(\theta_i) \in \mathbb{C}^{LK \times 1}$ is

$$\boldsymbol{\psi}(\theta_i) = \begin{pmatrix} \mathbf{h}_0(\theta_i) \\ \mathbf{h}_1(\theta_i) \\ \vdots \\ \mathbf{h}_{L-1}(\theta_i) \end{pmatrix}. \tag{38}$$

Such a reshaping of the data is beneficial, both to be able to use matrix manipulation and, more importantly, to hide the wideband DOA coupling term within the same dimension by stacking element indices l and fast-time samples k together. Thus, the matrix $\alpha_i \mathbf{f}_d(v_i)[\mathbf{a}(\theta_i) \otimes \mathbf{f}(R_i) \odot \boldsymbol{\psi}(\theta_i)]^T$, which contains the wideband DOA coupling term, is a rank-one matrix. Similar to (24), we have

$$\begin{aligned}&||\alpha_i \mathbf{f}_d(v_i) \left[\mathbf{a}(\theta_i) \otimes \mathbf{f}_r(R_i) \odot \boldsymbol{\psi}(\theta_i)\right]^T \odot \left[\mathbf{1}_L^T \otimes \boldsymbol{\Phi}(v_i)\right] ||_2 \\ &\quad \leq ||\alpha_i \mathbf{f}_d(v_i) \left[\mathbf{a}(\theta_i) \otimes \mathbf{f}_r(R_i) \odot \boldsymbol{\psi}(\theta_i)\right]^T ||_2.\end{aligned} \tag{39}$$

$\check{v}_i$ can be estimated through a one-dimensional search as

$$\check{v}_i = \underset{v}{\operatorname{argmax}} ||\mathbf{V}_i \odot [\mathbf{1}_L^T \otimes \boldsymbol{\Phi}^*(v)]||_2. \tag{40}$$

Next we focus on the efficient solution of (40). Although there is a default $norm$ function in MATLAB, it is not optimised for our specific problem. Let $\boldsymbol{\Lambda}_i(\check{v}_i) = \mathbf{V}_i \odot [\mathbf{1}_L^T \otimes \boldsymbol{\Phi}^*(\check{v}_i)]$, such that

$$||\boldsymbol{\Lambda}_i(\check{v}_i)||_2 = \sqrt{||\boldsymbol{\sigma}(\boldsymbol{\Lambda}_i(\check{v}_i)\boldsymbol{\Lambda}_i^H(\check{v}_i))||_{\max}}. \tag{41}$$

The solution of the spectral norm is transformed into the estimation of the largest eigenvalue of the matrix $\boldsymbol{\Lambda}_i(\check{v}_i)\boldsymbol{\Lambda}_i^H(\check{v}_i)$. Thus, compared to (21), another benefit of (36) is that the smallest dimension of the data matrix is shrunk to reduce the computational load of calculating the spectral norm. There are many algorithms to perform the eigendecomposition of a Hermitian matrix; here we propose using the simple power iteration algorithm since only the largest eigenvalue is needed [44]. Moreover, the compensations in the adjacent searching grids are just a minor phase shift, thus the eigenvectors associated with the largest eigenvalues for the neighbouring searching grids are close to each other in the norm. According to the simulation, after good initialisation, only a few power iterations are required to provide a sufficiently good

Algorithm 5: Power Iteration (**A5**).

Input: Hermitian matrix $\mathbf{R}$, $\mathbf{u}^{(0)}$ with $||\mathbf{u}^{(0)}|| = 1$, $j = 0$
repeat
  $\mathbf{w} \Leftarrow \mathbf{R}\mathbf{u}^{(j)}$
  $\mathbf{u}^{(j+1)} \Leftarrow \mathbf{w}/||\mathbf{w}||$
  $\lambda^{(j+1)} \Leftarrow (\mathbf{u}^{(j+1)})^H \mathbf{R}\mathbf{u}^{(j+1)}$
  $j \Leftarrow j + 1$
until $|\lambda^{(j)} - \lambda^{(j-1)}| < \delta$, δ is the presetting threshold
Output: $\mathbf{u}^{(j)}$, $\lambda^{(j)}$

Algorithm 6: Efficient Implementation of (40) (**A6**).

Initialize $\mathbf{u}^{(0)} = [1, 0, 0, \ldots, 0] \in \mathbb{R}^{M\times 1}$, empty vector $\boldsymbol{\lambda} = \varnothing$, searching domain $\check{\mathbf{v}} = -V : \Delta v : V$, $j = 0$
for v in $\check{\mathbf{v}}$ **do**
  $\mathbf{R} \Leftarrow \boldsymbol{\Lambda}_i(v)\boldsymbol{\Lambda}_i^H(v)$
  Compute $\lambda^{(j+1)}$ and $\mathbf{u}^{(j+1)}$ using **A5** with input $\mathbf{R}$ and $\mathbf{u}^{(j)}$
  Store the eigenvalue $[\boldsymbol{\lambda}]_j \Leftarrow \lambda^{(j+1)}$
  $j \Leftarrow j + 1$
end for
Find index q of $||\boldsymbol{\lambda}||_{\max}$ in $\boldsymbol{\lambda}$
Output: $[\check{\mathbf{v}}]_q$

largest eigenvalue approximation with the previous eigenvector as the initial estimation. To make this paper self-contained, the power iteration algorithm is given in Algorithm 5 (**A5**).

Based on the analysis, the efficient implementation of (40) is shown in Algorithm 6 (**A6**), where the velocity searching domain $\check{\mathbf{v}}$ is $-V : \Delta v : V$ (sampled with the linear spacing Δv).

Similarly, the angle $\check{\theta}_i$ can be estimated by stacking the slow-time and the fast-time dimensions together from (17). The derivations are straightforward and are omitted here.

VI. Simulations

In this section, several numerical examples are presented to demonstrate the effectiveness of the proposed algorithm.

The conventional coherent-integration method found by replacing step 1 in **A2** with (18) (the FFT-based algorithm) is compared with the proposed new algorithm in terms of accuracy and time consumption. The RMSE is obtained from 400 Monte-Carlo trials as RMSE $= \sqrt{\mathbb{E}[(\tilde{\vartheta} - \vartheta)^2]}$, where $\tilde{\vartheta}$ denotes the estimated parameter and ϑ is its true value. The starting frequency of the FMCW waveform is $f_0 = 77$ GHz, and the chirp duration is $T_0 = 0.08$ ms. The chirp repetition interval is $T_r = 0.1$ ms and $M = 8$ chirps data are collected for simulation, so the total CPI is 0.8 ms. Therefore, within such a short time, all the targets are moving with approximately constant velocities. A standard ULA of $L = 8$ elements with the inter-element distance of $d = \frac{c}{2f_0} \approx 0.195$ mm is considered for receivers. According to the parameters, the unambiguous velocity domain is $[-v_{\max}, v_{\max})$ with $v_{\max} \approx 9.7$ m/s. Unless otherwise stated, the alternation in **A2** is repeated $\beta = 3$ times as default; the default bandwidth is set as $B = 4$ GHz, which means the theoretical range resolution is $\Delta r = \frac{c}{2B} \approx 0.037$ m; the magnitudes of the targets follow $|\alpha_i| \sim \mathcal{U}(0.5, 1)$ and remain constant over the observation time; the threshold ϵ_1 is set as $0.2 \times |\tilde{\alpha}_1|$ and ϵ_2 is set as $0.4 \times |\tilde{\alpha}_1|$, where $|\tilde{\alpha}_1|$ is the estimated magnitude of the first target and usually is the largest magnitude among all targets; the velocities of the targets are set randomly and follow $v_i \sim \mathcal{U}(-6v_{\max}, 6v_{\max})$. The SNR is defined as SNR $= \frac{||\sum_{i=1}^{I} \mathbf{X}_i \odot \boldsymbol{\Omega}_{\theta r}(\theta_i) \odot \boldsymbol{\Omega}_{dr}(v_i)||_F^2}{||\mathbf{N}||_F^2}$.

A. Multiple Targets Simulation and Time Consumption Comparison

In the first case study, the general estimation performance of the proposed norm-based method and that of the FFT-based method are compared. Ten random point-like moving targets are set in the observation scene and illuminated by the FMCW waveform. The reflected signals collected with the antenna array are sampled with a sampling frequency $f_s = 640$ kHz ($K = 512$ snapshots for each fast-time), and the SNR is set to 10 dB. The simulation results are shown in Fig. 2, where the labels in the legend are: *FFT* denotes the FFT-based algorithm, *Norm* denotes the proposed spectral norm algorithm and implemented by default *norm* function, and *PI* denotes the proposed algorithm implemented by power iteration.

Here, to illustrate the off-grid problem of the FFT-based method, two sets of simulation for this method are performed with $\kappa - 1$ times zero-padding (κ times FFT points). In the first case, (18) is applied with 1-time ($\kappa = 2$) zero-padding. The angle-range and range-velocity results are shown in Fig. 2(a)(b), respectively. Since the DOAs have no ambiguity problem for the system, despite minor errors, the DOAs are almost correctly estimated. However, most of the velocity estimates have large errors due to the off-grid problem.

The situation is better when the number of zero-paddings is increased to 3 times ($\kappa = 4$). The results are shown in Fig. 2(c)(d), where 2 targets still appear with incorrect ambiguity number estimation. Although it can be expected that better results can be obtained by increasing κ, the time- and memory-consumption become unacceptable for applications in mind.

Fig. 2(e)(f) and Fig. 2(g)(h) show much more accurate estimation of the scene by using the proposed norm-based methods with and without power iteration, respectively. The estimation of the angles is more accurate than that in Fig. 2(a)(c), and there is no estimation error of fold number in Fig. 2(f)(h). Additionally, the proposed efficient implementation has similar performance with the default $norm$ function. Since the range-Doppler spectra are almost identical in all fold numbers if the narrowband processing algorithm is applied, the Doppler ambiguity cannot be resolved and all targets will be detected in different fold numbers as shown in Fig. 3.

The estimation error of fold number $\sum_{i=1}^{I} |n_i - \tilde{n}_i|$ and the RMSEs of unambiguous velocity are shown in Fig. 4. Here we assume that the number of targets I is known. It is shown that for 10 far-separated targets, the error of the fold number estimation using the proposed methods converges to 0 within 3 iterations, while that using FFT-based algorithm with 3 times

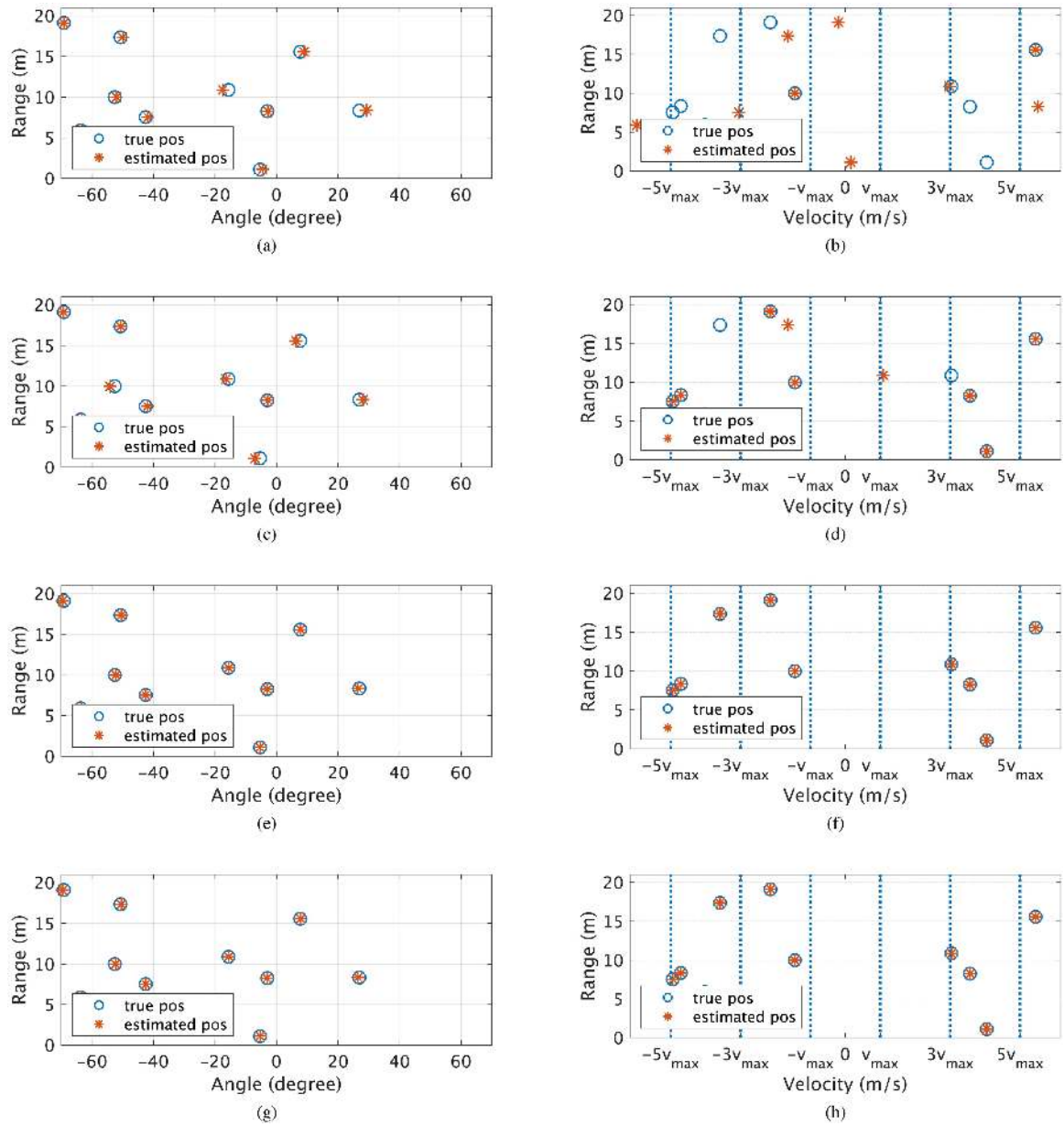

Fig. 2. Angle-range and velocity-range maps for (a) (b) FFT-based algorithm with 1 ($\kappa = 2$) time zero-padding, (c) (d) FFT-based algorithm with 3 ($\kappa = 4$) times zero-paddings, (e) (f) proposed norm-based method, (g) (h) proposed efficient implementation.

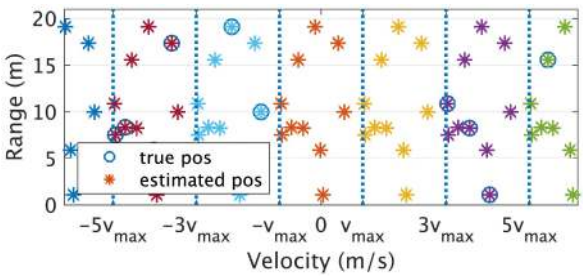

Fig. 3. Velocity-range map for narrowband signal model.

zero-paddings ($\kappa = 4$) converges to 2, and with 1-time zero-padding ($\kappa = 2$) cannot converge to a stable point but keeps fluctuating significantly with iterations. The RMSEs of unambiguous velocity estimation in Fig. 4(b) strongly correspond to the estimation errors of the fold number in Fig. 4(a), while the proposed spectral norm-based algorithms with and without efficient implementation can reach 0 errors in fold number estimation. Additionally, the proposed algorithm with only $\beta = 1$ alternation in $\mathbf{A}2$ is also applied, and the simulation results in Fig. 4 demonstrate that with more alternations in $\mathbf{A}2$, $\mathbf{A}4$ can converge more quickly.

In addition to the increased accuracy of the proposed algorithm, the comparison of the time consumption of different algorithms is listed in Table I. The simulation results show that when implemented with power iteration, the proposed algorithm is preferable for both accuracy and efficiency. We note that 3-dimensional FFT is applied to the cubic data and the zero-padding is applied to all dimensions. Therefore, the time is approximately increased $2^3 = 8$ times when κ doubles.

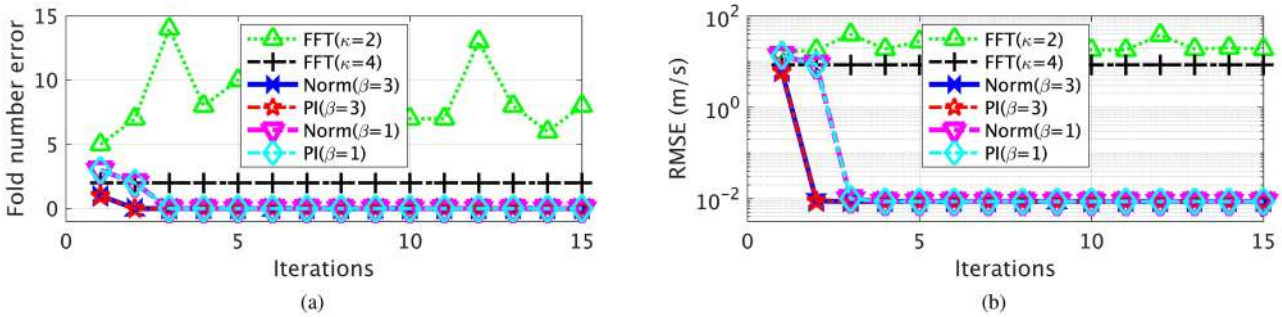

Fig. 4. (a) Fold number estimation errors with iteration, (b) RMSEs of ambiguous velocities with iteration.

TABLE I
TIME CONSUMPTION COMPARISON

Algorithm	Norm-based (power iteration)	Norm-based (default $norm$ function)	FFT-based ($\kappa = 2$)	FFT-based ($\kappa = 4$)
A2 seconds	12.70	19.07	31.14	217.79
A3 seconds per iteration	8.27	9.77	13.57	54.45

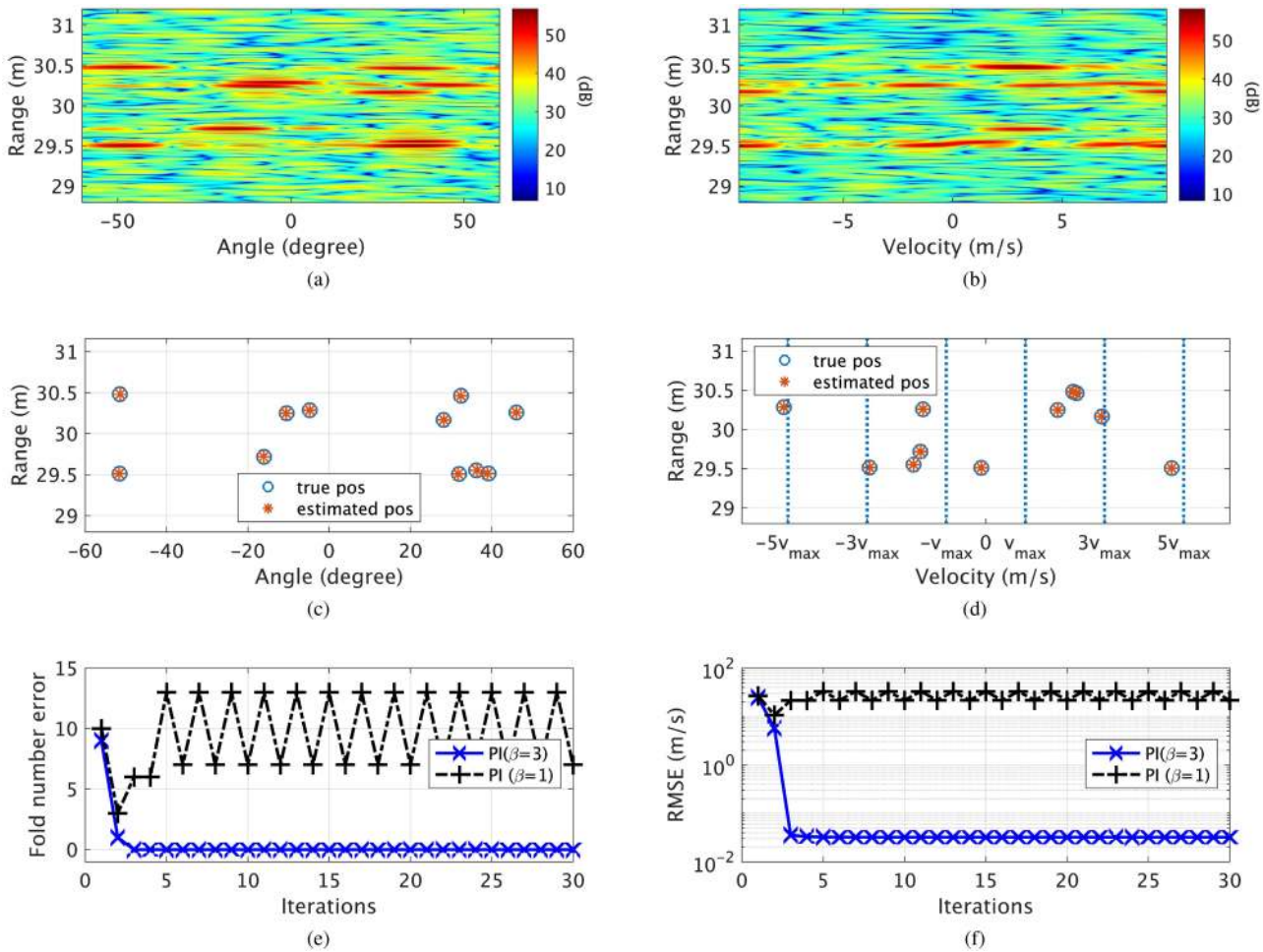

Fig. 5. Simulation results: (a) angle-range spectrum for $M = 0$, (b) range-velocity spectrum for $L = 0$, (c) angle-range map using proposed algorithm with power iteration, (d) velocity-range map using proposed algorithm with power iteration, (e) fold number errors with different alternations and (f) RMSEs of ambiguous velocity estimation with different alternations.

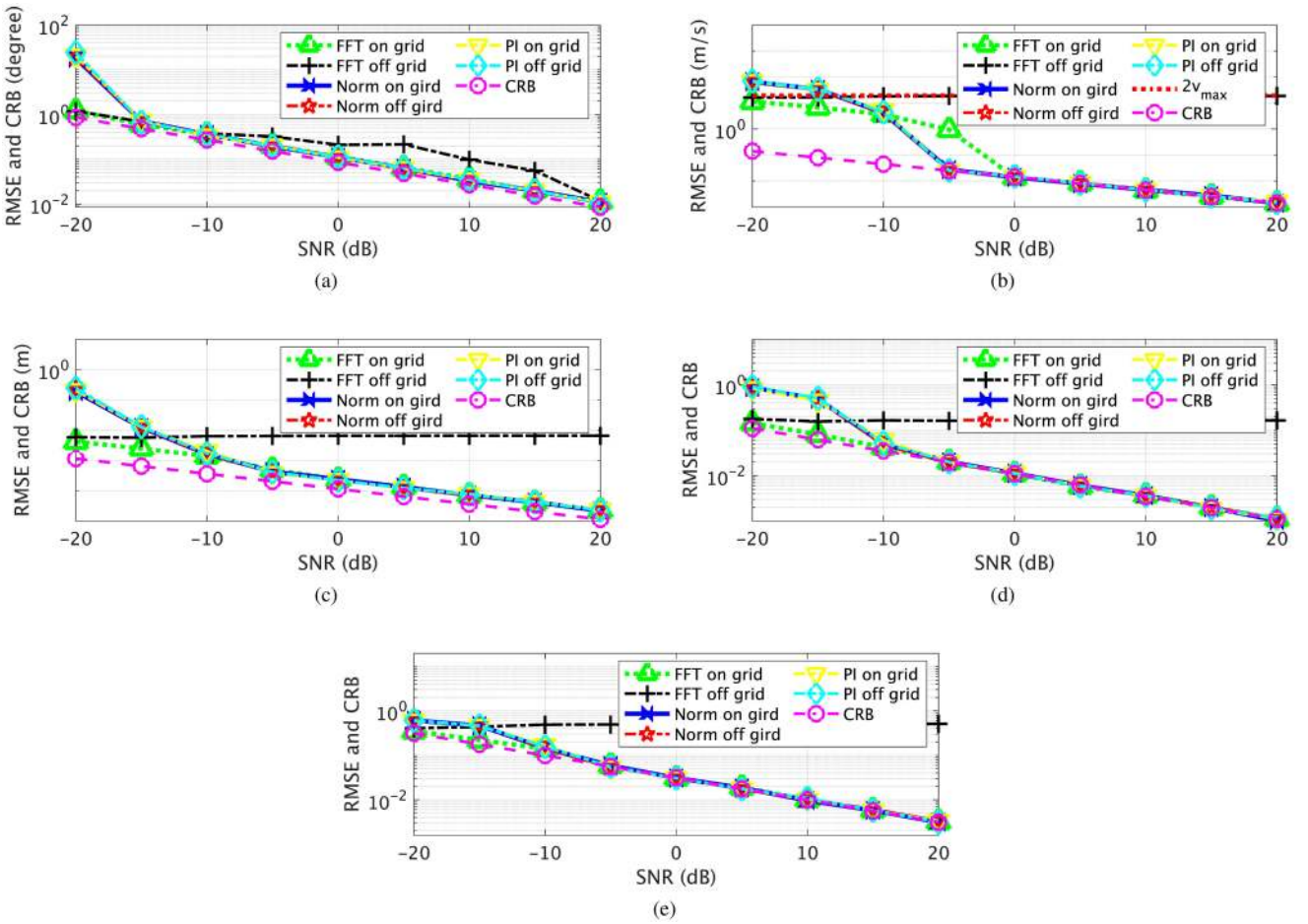

Fig. 6. RMSEs and CRB comparisons for a single point-like target of (a) angle $\tilde{\theta}$, (b) velocity $\tilde{v}$, (c) range $\tilde{r}$, (d) real part and (e) imaginary part of the amplitude $\tilde{\alpha}$.

Moreover, the full-dimensional FFT has to been applied multiple times on (v, θ) map, that is why the time consumption of (18) is super high.

B. Low SNR With Different Alternations

The previous simulation has shown that **A**2 can accelerate the convergence of **A**4. In this subsection, the superiority of **A**2 under low SNR condition with multiple targets is presented as well. To reduce the integrated SNR, the fast-time snapshots are decreased to $K = 64$ and SNR is set to SNR $= 5$ dB. The other 11 point-like targets are randomly positioned in the observation scene. The results of applying FFT to the raw data of the first slow-time sample ($M = 0$) and the first antenna element ($L = 0$) are shown in Fig. 5(a)(b), in which the migration phenomenon is hardly seen from the range-velocity map. The estimation results with the proposed algorithm are shown in Fig. 5(c)(d). The proposed algorithm can estimate all the targets with high accuracy. Then, to prove the importance of **A**2, the alternation is decreased to $\beta = 1$ repeat. The corresponding fold number estimation error and the RMSEs of the unambiguous velocities are plotted in Fig. 5(e)(f). Without sufficient alternations, **A**4 cannot reach convergence, while with only $\beta = 3$ repeats of **A**2, **A**4 converges within 5 iterations.

C. RMSE Comparison of Norm Versus FFT

To show the off-grid problem more clearly, two sets of simulations are performed for only one target, which is either an on-grid target or an off-grid one. To save the simulation time on Monte Carlo trials, the fast-time snapshots are set to $K = 64$. The parameters for the on-grid target are $R = 16\frac{\Delta r}{\kappa}$, $v = 20\frac{2v_{\max}}{\kappa M}$, $\theta = 40^\circ$ and the off-grid target is located between the two FFT grids both for range and velocity as $R = 16.5\frac{\Delta r}{\kappa}$, $v = 20.5\frac{2v_{\max}}{\kappa M}$ and $\theta = 40^\circ$, where κ means $\kappa - 1$ times zero-paddings for (18).

The RMSEs and the corresponding CRB comparisons are shown in Fig. 6 for $\kappa = 4$ (see Appendix A for CRB derivation). One can see from Fig. 6 that for the on-grid target, both norm-based and FFT-based algorithms can reach the CRBs for all parameters. It is also observed that the proposed method can reach the CRB at approximately -5dB for the ambiguous velocity, while the FFT-based algorithm reaches the CRB at around 0 dB. We have to stress here that the estimates are refined using Nelder-Mead method in the last step of **A**2, so the estimates

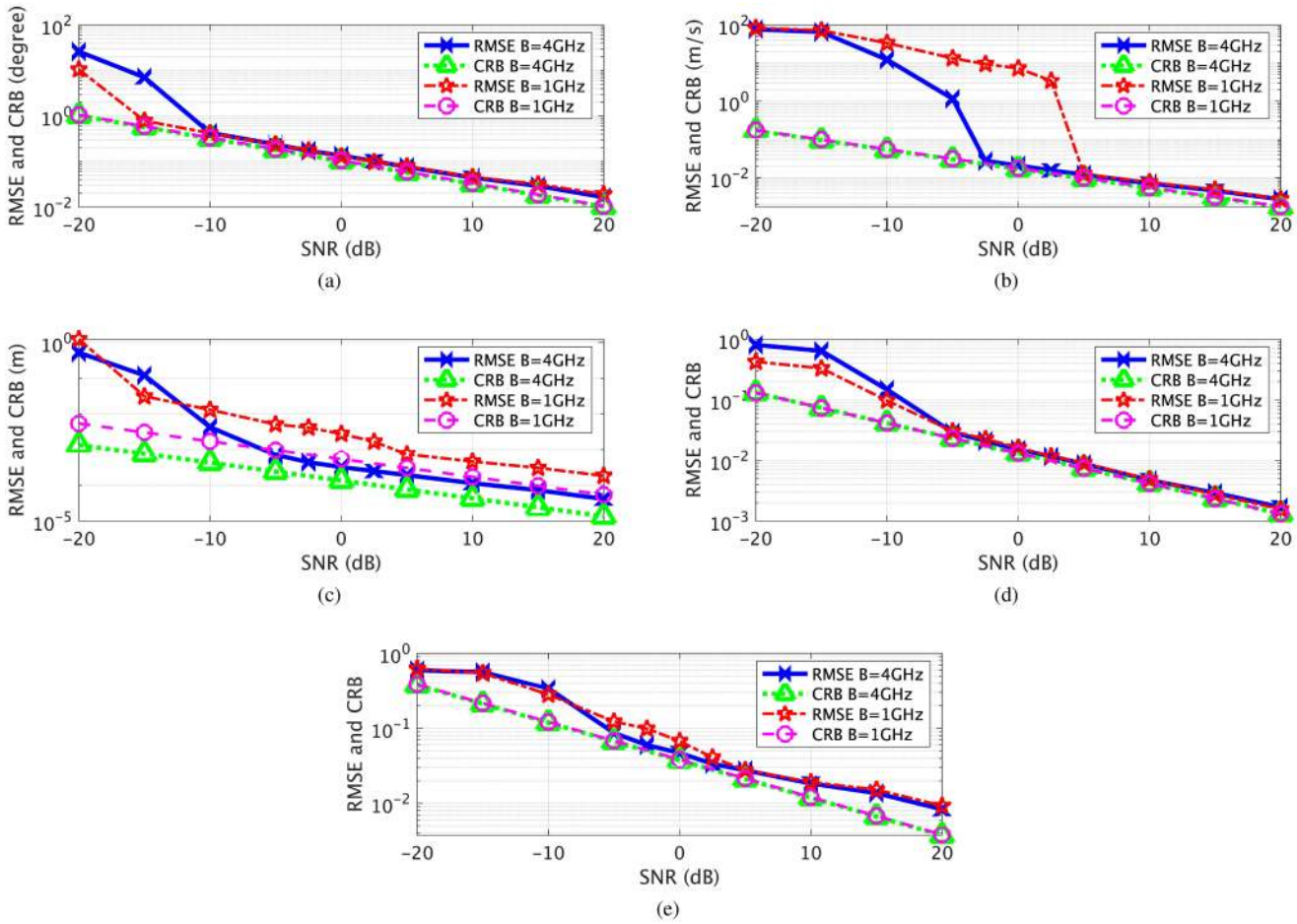

Fig. 7. RMSEs and CRB comparisons for two far-separated targets of (a) angle $\tilde{\theta}$, (b) velocity $\tilde{v}$, (c) range $\tilde{r}$, (d) real part and (e) imaginary part of the amplitude $\tilde{\alpha}$.

of on-grid targets are gridless and the accuracy will be influenced by the SNR accordingly.

Nonetheless, we must admit that under conditions of very low SNR, coherent integration methods may have better estimation performance than the proposed method, since the RMSEs of the FFT-based method are much lower than that of the proposed algorithm for SNR in $(-20, -10)$dB.

Considering the off-grid target, the RMSE of the velocity using the FFT-based method cannot reach the CRB but keeps an approximately constant value of $2v_{\max}$. This is because the fold number is estimated incorrectly. The wrong estimation of the unambiguous velocity decreases the accuracy of the DOA, range and amplitude as well.

D. RMSE Comparison of Bandwidth 1 GHz Versus 4 GHz

From the signal model we can speculate that with a larger bandwidth, the phase of the coupling terms will vary more significantly and therefore will have a higher SNR tolerance. This means that under low SNR conditions, the parameters extraction from the coupling terms are more accurate with a larger bandwidth. Thus, in this study, the performance of the proposed method is tested with different bandwidths, namely 1 GHz and 4 GHz. Two separate targets are set in the observation scene. The parameters of two targets are $\mathbf{v} = [50, 60]$, $\boldsymbol{\theta} = [30^\circ, 10^\circ]$, $\mathbf{r} = [0.5, 0.8]$, respectively.

Fig. 7 gives the results of the RMSEs and the corresponding CRB comparisons. According to Fig. 7, the performances for angle and amplitude are almost identical which demonstrates that the proposed method is adaptive to signals with different bandwidths for DOA estimation. It is also observed that the CRB of the range with 4 GHz is lower than that with 1 GHz simply because the wider frequency band provides a higher range resolution. Furthermore, with the 4 GHz signal, the RMSE of the unambiguous velocity reaches the CRB from the lower SNR condition of -2.5 dB, while that with the 1 GHz signal reaches the CRB from approximately 5 dB. The simulation results indicate that a possible way to resolve the fold number under very low SNR conditions with constrained data size could be to increase the bandwidth.

E. RMSEs of Closely Positioned Targets

The super-resolution ability of RELAX method has been shown in [5]. While the proposed method is applied to a more general signal model, the estimation performance for closely positioned targets is evaluated in numerical simulations in this subsection. Two targets with the same angles and Doppler shifts

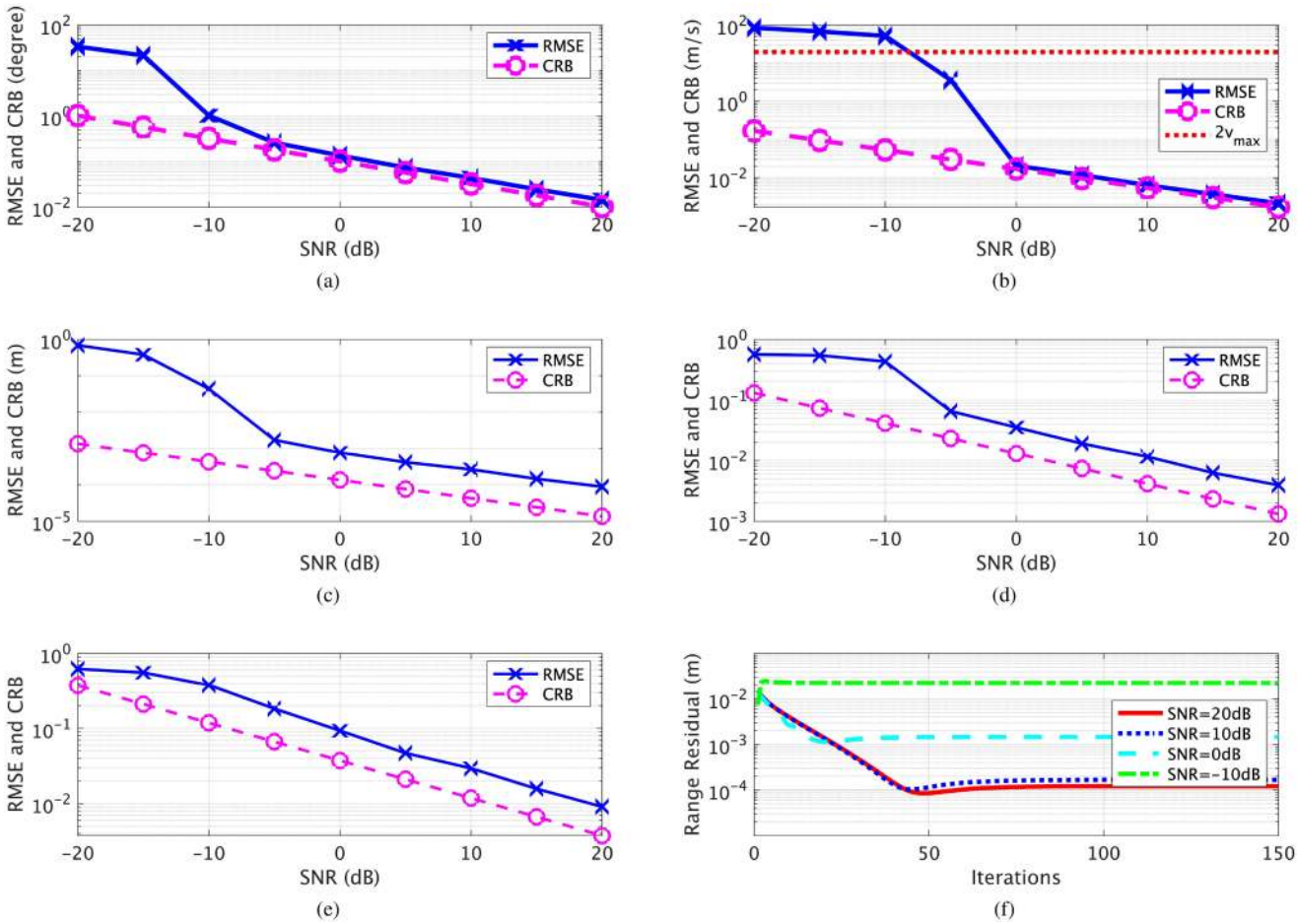

Fig. 8. RMSEs and CRB comparisons for two close targets of (a) angle $\tilde{\theta}$, (b) velocity $\tilde{v}$, (c) range $\tilde{r}$, (d) real part and (e) imaginary part of the amplitude $\tilde{\alpha}$, and (f) the range residual with iteration number.

but half the range resolution distances are set in the observation scene. The parameters are $\mathbf{v} = [50, 50]$, $\boldsymbol{\theta} = [30^\circ, 30^\circ]$, $\mathbf{r} = [0.5, 0.5 + \frac{\Delta_r}{2}]$, respectively.

The comparisons of the RMSEs and the corresponding CRBs using the proposed algorithm with efficient implementation are shown in Fig. 8(a)–(e). Although the performance is not as good as that for two far-separated targets, as shown in Fig. 7, the RMSEs of all the parameters decrease along with the CRB when SNR ≥ 0 dB. Of all parameters, the RMSE of unambiguous velocity estimation has the best performance and almost reaches the CRB.

Moreover, the RMSE trends and the simulation results show that the two closely spaced targets are successfully resolved from each other, which validates that the proposed algorithm holds the super-resolution ability of **A**4. It is worth noting that for the closely positioned targets, far more iterations (around 50 iterations) are needed for convergence. The range residuals of the iterations are plotted in Fig. 8(f), where the range residual of pth iteration is defined as $||\tilde{\mathbf{r}}^{(p)} - \tilde{\mathbf{r}}^{(p-1)}||$.

VII. Conclusion

In this paper, the joint features extraction of multiple fast-moving targets from UWB FMCW signals, taking both Doppler ambiguity and wideband DOA problems into account, is considered. A novel spectral norm-based algorithm is proposed, with which to estimate the coupling terms caused by range migration and wideband DOA for a single target and to subsequently resolve the Doppler ambiguity through a series of approaches. Combined with the greedy and RELAX algorithms, the proposed method is extended to the multiple moving targets scenario. For the algorithm **A**2, the convergence is obvious. As for **A**3 and **A**4, the greedy and RELAX algorithms in **A**3 and **A**4 have been widely used in many studies [5], [7], [38]–[43], and we refer to those papers for detailed discussions on their convergence. Furthermore, an efficient implementation of the proposed method is introduced using power iteration.

The performance of the proposed algorithm concerning the accuracy of the estimated parameters is compared to CRB. The simulation results demonstrate that the proposed algorithm outperforms the conventional coherent integration-based method both in accuracy and efficiency with moderate data size. Finally, the super-resolution ability of the RELAX is held at the expense of the slight loss of the accuracy and larger number of iterations. The performance of the proposed algorithm will be tested or improved in more demanding scenarios, for instance, non-Gaussian noise or strong clutters. Also, the proposed algorithm will be applied to real data in our future work.

APPENDIX A
CRB DERIVATION

To formulate the CRB matrix, we first reshape the raw data (13) into the vector form $\mathbf{y} \in \mathbb{C}^{LMK\times 1}$ as

$$\mathbf{y} = \sum_{i=1}^{I} \alpha_i(\mathbf{a}(\theta_i) \otimes \mathbf{f}_d(v_i) \otimes \mathbf{f}_r(R_i)) \odot \boldsymbol{\omega}_{\theta r}(\theta_i) \odot \boldsymbol{\omega}_{dr}(v_i) + \mathbf{n}, \tag{42}$$

where all the Doppler velocities are considered as unambiguous, and $\boldsymbol{\omega}_{dr}(v_i) \in \mathbb{C}^{LMK\times 1}$ and $\boldsymbol{\omega}_{\theta r}(\theta_i) \in \mathbb{C}^{LMK\times 1}$ are

$$\boldsymbol{\omega}_{dr}(v_i) = \mathbf{1}_L \otimes \begin{pmatrix} \mathbf{g}_0(v_i) \\ \mathbf{g}_1(v_i) \\ \vdots \\ \mathbf{g}_{M-1}(v_i) \end{pmatrix}, \boldsymbol{\omega}_{\theta r}(\theta_i) = \begin{pmatrix} \mathbf{1}_M \otimes \mathbf{h}_0(\theta_i) \\ \mathbf{1}_M \otimes \mathbf{h}_1(\theta_i) \\ \vdots \\ \mathbf{1}_M \otimes \mathbf{h}_{L-1}(\theta_i) \end{pmatrix}. \tag{43}$$

Let $\mathbf{Q} \in \mathbb{C}^{LMK\times LMK}$ be the noise covariance matrix, which is

$$\mathbf{Q} = E(\mathbf{n}\mathbf{n}^H) = \sigma^2 \mathbf{I}_{MLK}, \tag{44}$$

with σ^2 being the variances of the noise. According to the extended Slepian-Bangs' formula [45], the ijth element of the fisher information matrix (FIM) has the form

$$\{\text{FIM}\}_{ij} = \text{Tr}\left(\mathbf{Q}^{-1}\frac{\partial \mathbf{Q}}{\partial \boldsymbol{\eta}_i}\mathbf{Q}^{-1}\frac{\partial \mathbf{Q}}{\partial \boldsymbol{\eta}_j}\right) + 2\Re\left[\left(\frac{\partial \mathbf{y}}{\partial \boldsymbol{\eta}_i}\right)^H \mathbf{Q}^{-1}\left(\frac{\partial \mathbf{y}}{\partial \boldsymbol{\eta}_j}\right)\right], \tag{45}$$

where

$$\boldsymbol{\eta} = [\boldsymbol{\theta}, \mathbf{v}, \mathbf{r}, \Re(\boldsymbol{\alpha}), \Im(\boldsymbol{\alpha})]^T, \tag{46}$$

where $\partial \mathbf{y}/\partial \boldsymbol{\eta}_i$ denotes the derivative of $\mathbf{y}$ with respect to the ith parameter of $\boldsymbol{\eta}$. Note that the FIM is block diagonal since the parameters in $\mathbf{Q}$ are independent of those in $\boldsymbol{\eta}$ and vice versa. Thus, the CRB matrix for the motion parameters can be calculated from the second term on the right side of (45). The derivations of each parameter are given as follows, where for simplicity the denotations are ignored.

$$\boldsymbol{\chi}_i^{\theta} = j\xi_{1,i}(\mathbf{d}_L \odot \mathbf{a}) \otimes \mathbf{f}_d \otimes \mathbf{f}_r \odot \boldsymbol{\omega}_{dr} \odot \boldsymbol{\omega}_{\theta r} + j\xi_{2,i}\mathbf{a} \otimes \mathbf{f}_d \otimes \mathbf{f}_r \odot \boldsymbol{\omega}_{dr} \odot [\boldsymbol{\omega}_{\theta r} \odot (\mathbf{d}_L \otimes \mathbf{1}_M \otimes \mathbf{d}_K)], \tag{47a}$$

$$\boldsymbol{\chi}_i^{\mathbf{v}} = j\zeta_{1,i}\mathbf{a} \otimes (\mathbf{d}_M \odot \mathbf{f}_d) \otimes \mathbf{f}_r \odot \boldsymbol{\omega}_{dr} \odot \boldsymbol{\omega}_{\theta r} + j\zeta_{2,i}\mathbf{a} \otimes \mathbf{f}_d \otimes \mathbf{f}_r \odot [(\mathbf{1}_L \otimes \mathbf{d}_M \otimes \mathbf{d}_K) \odot \boldsymbol{\omega}_{dr}] \odot \boldsymbol{\omega}_{\theta r}, \tag{47b}$$

$$\boldsymbol{\chi}_i^{\mathbf{r}} = j\nu\mathbf{a} \otimes \mathbf{f}_d \otimes (\mathbf{d}_K \odot \mathbf{f}_r) \odot \boldsymbol{\omega}_{dr} \odot \boldsymbol{\omega}_{\theta r}, \tag{47c}$$

$$\boldsymbol{\alpha}_i^{\Re} = \mathbf{a} \otimes \mathbf{f}_d \otimes \mathbf{f}_r \odot \boldsymbol{\omega}_{dr} \odot \boldsymbol{\omega}_{\theta r}, \tag{47d}$$

$$\boldsymbol{\alpha}_i^{\Im} = j\mathbf{a} \otimes \mathbf{f}_d \otimes \mathbf{f}_r \odot \boldsymbol{\omega}_{dr} \odot \boldsymbol{\omega}_{\theta r}, \tag{47e}$$

where the coefficients are $\xi_{1,i} = 2\pi\alpha_i f_0 \frac{d}{c}\cos\theta_i$, $\xi_{2,i} = 2\pi\alpha_i\mu\frac{d}{cf_s}\cos\theta_i$, $\zeta_{1,i} = -4\pi\alpha_i T\frac{f_0}{c}$, $\zeta_{2,i} = -4\pi\alpha_i T\frac{\mu}{cf_s}$ and $\nu = 4\pi\frac{\mu}{cf_s}$. Let

$$\mathbf{G} = [\boldsymbol{\chi}_1^{\theta} \cdots \boldsymbol{\chi}_I^{\theta}, \boldsymbol{\chi}_1^{\mathbf{v}} \cdots \boldsymbol{\chi}_I^{\mathbf{v}}, \boldsymbol{\chi}_1^{\mathbf{r}}, \cdots \boldsymbol{\chi}_I^{\mathbf{r}}, \boldsymbol{\alpha}_1^{\Re} \ldots \boldsymbol{\alpha}_I^{\Re}, \boldsymbol{\alpha}_1^{\Im} \ldots \boldsymbol{\alpha}_I^{\Im}]. \tag{48}$$

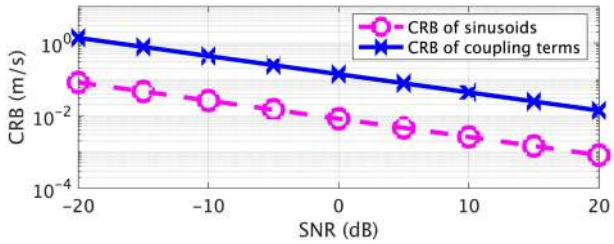

Fig. 9. CRB comparison of folded velocity from sinusoids and the unambiguous velocity from the coupling terms.

Then the CRB matrix for the parameter vector $\boldsymbol{\eta}$ is given by

$$CRB(\boldsymbol{\eta}) = [2\Re(\mathbf{G}^H\mathbf{Q}^{-1}\mathbf{G})]^{-1}. \tag{49}$$

APPENDIX B
CRB OF VELOCITIES

There are two terms in (47b), where the first term is the derivation of folded velocity from the sinusoids and the second term is the derivation of unambiguous velocity from the coupling terms. Therefore, the corresponding CRBs can be calculated separately. Let $\hat{\boldsymbol{\chi}}_i^{\mathbf{v}} = j\zeta_{1,i}\mathbf{a} \otimes (\mathbf{d}_M \odot \mathbf{f}_d) \otimes \mathbf{f}_r \odot \boldsymbol{\omega}_{dr} \odot \boldsymbol{\omega}_{\theta r}$ and $\check{\boldsymbol{\chi}}_i^{\mathbf{v}} = j\zeta_{2,i}\mathbf{a} \otimes \mathbf{f}_d \otimes \mathbf{f}_r \odot [(\mathbf{1}_L \otimes \mathbf{d}_M \otimes \mathbf{d}_K) \odot \boldsymbol{\omega}_{dr}] \odot \boldsymbol{\omega}_{\theta r}$. Then set $\mathbf{G} = [\hat{\boldsymbol{\chi}}_1^{\mathbf{v}}; \ldots, \hat{\boldsymbol{\chi}}_I^{\mathbf{v}}]$ or $\mathbf{G} = [\check{\boldsymbol{\chi}}_1^{\mathbf{v}}, \ldots, \check{\boldsymbol{\chi}}_I^{\mathbf{v}}]$, the corresponding CRBs can be calculated according to (49) for $\hat{\mathbf{v}}$ or $\check{\mathbf{v}}$.

Using the same system setting from Section VI-C, and with one target set as $\alpha = 1$, $v = 50$ m/s, $R = 30$ m and $\theta = 30°$, the corresponding CRBs for $\hat{v}$ and $\check{v}$ are plotted in Fig. 9.

ACKNOWLEDGMENT

The authors would like to thank the China Scholarship Council (CSC) for the PhD scholarship for the first author. The authors would also like to thank Dr. Nikita Petrov for many constructive discussions and helpful suggestions. Finally, the authors appreciate the Associate Editor and anonymous reviewers for their constructive comments based on which the presentation of this paper has been significantly improved.

REFERENCES

[1] S. A. Rane, S. Sarkar, and A. Gaurav, "Moving target localization using ultra wideband sensing," in *Proc. Int. Conf. Green Eng. Technol. (IC-GET)*, Nov. 2016, pp. 1–5.
[2] F. Deudon, F. Le Chevalier, S. Bidon, O. Besson, and L. Savy, "A migrating target indicator for wideband radar," in Proc. *IEEE Sensor Array Multichannel Signal Process. Workshop*, 2010, pp. 249–252.
[3] F. Dai, H. Liu, P. Shui, and S. Wu, "Adaptive detection of wideband radar range spread targets with range walking in clutter," *IEEE Trans. Aerosp. Electron. Syst.*, vol. 48, no. 3, pp. 2052–2064, Jul. 2012.
[4] S. Xu, B. J. Kooij, and A. Yarovoy, "Joint Doppler and DOA estimation using (ultra-)wideband FMCW signals," *Signal Process.*, vol. 168, 2020, Art. no. 107259, doi: 10.1016/j.sigpro.2019.107259.
[5] N. Jiang, R. Wu, and J. Li, "Super resolution feature extraction of moving targets," *IEEE Trans. Aerosp. Electron. Syst.*, vol. 37, no. 3, pp. 781–793, Jul. 2001.

[6] Z. Sun, X. Li, W. Yi, G. Cui, and L. Kong, "Detection of weak maneuvering target based on Keystone transform and matched filtering process," *Signal Process.*, vol. 140, pp. 127–138, 2017. [Online]. Available: https://www.sciencedirect.com/science/article/pii/S0165168417301846
[7] J. Li, G. Liu, N. Jiang, and P. Stoica, "Moving target feature extraction for airborne high-range resolution phased-array radar," *IEEE Trans. Signal Process.*, vol. 49, no. 2, pp. 277–289, Feb. 2001.
[8] S. Xu and A. Yarovoy, "Joint parameters estimation using 3D tensor MUSIC in the presence of phase residual," in *Proc. Int. Conf. Radar*, Aug. 2018, pp. 1–4.
[9] N. Petrov and F. L. Chevalier, "Iterative adaptive approach for unambiguous wideband radar target detection," in *Proc. Eur. Radar Conf.*, Sep. 2015, pp. 45–48.
[10] I. Shapir, I. Bilik, and G. Barkan, "Doppler ambiguity resolving in TDMA automotive MIMO radar via digital multiple PRF," in *Proc. IEEE Radar Conf.*, 2018, pp. 175–180.
[11] H. Rohling and M.-M. Meinecke, "Waveform design principles for automotive radar systems," in *Proc. CIE Int. Conf. Radar*, 2001, vol. 4, p. 1.
[12] S. Bidon, J.-Y. Tourneret, L. Savy, and F. Le Chevalier, "Bayesian sparse estimation of migrating targets for wideband radar," *IEEE Trans. Aerosp. Electron. Syst.*, vol. 50, no. 2, pp. 871–886, Apr. 2014.
[13] S. Bidon, O. Besson, J. Tourneret, and F. Le Chevalier, "Bayesian sparse estimation of migrating targets in autoregressive noise for wideband radar," in *Proc. IEEE Radar Conf.*, May 2014, pp. 0579–0584.
[14] S. Bidon, A. Tamalet, and J. Tourneret, "Variational bayesian inference for sparse representation of migrating targets in wideband radar," in *Proc. IEEE Radar Conf.*, Apr. 2013, pp. 1–5.
[15] B. D. Carlson, E. D. Evans, and S. L. Wilson, "Search radar detection and track with the Houghtransform. I. system concept," *IEEE Trans. Aerosp. Electron. Syst.*, vol. 30, no. 1, pp. 102–108, Jan. 1994.
[16] F. Deudon, S. Bidon, O. Besson, and J.-Y. Tourneret, "Velocity dealiased spectral estimators of range migrating targets using a single low-PRF wideband waveform," *IEEE Trans. Aerosp. Electron. Syst.*, vol. 49, no. 1, pp. 244–265, Jan. 2013.
[17] X. Li, G. Cui, W. Yi, and L. Kong, "Sequence-reversing transform-based coherent integration for high-speed target detection," *IEEE Trans. Aerosp. Electron. Syst.*, vol. 53, no. 3, pp. 1573–1580, Jun. 2017.
[18] X. Li, G. Cui, W. Yi, and L. Kong, "Radar maneuvering target detection and motion parameter estimation based on TRT-SGRFT," *Signal Process.*, vol. 133, pp. 107–116, 2017, doi: 10.1016/j.sigpro.2016.10.014.
[19] J. Zheng, T. Su, W. Zhu, X. He, and Q. H. Liu, "Radar high-speed target detection based on the scaled inverse Fourier transform," *IEEE J. Sel. Topics Appl. Earth Observ. Remote Sens.*, vol. 8, no. 3, pp. 1108–1119, Mar. 2015.
[20] Z. Sun, X. Li, W. Yi, G. Cui, and L. Kong, "A coherent detection and velocity estimation algorithm for the high-speed target based on the modified location rotation transform," *IEEE J. Sel. Topics Appl. Earth Observ. Remote Sens.*, vol. 11, no. 7, pp. 2346–2361, Jul. 2018.
[21] Z. Dai, X. Zhang, H. Fang, and Y. Bai, "High accuracy velocity measurement based on Keystone transform using entropy minimization," *Chin. J. Electron.*, vol. 25, no. 4, pp. 774–778, 2016.
[22] Z. Sun, X. Li, W. Yi, G. Cui, and L. Kong, "Detection of weak maneuvering target based on KT-MFP," in *Proc. IEEE Radar Conf.*, 2017, pp. 1488–1492.
[23] J. Zheng, T. Su, H. Liu, G. Liao, Z. Liu, and Q. H. Liu, "Radar high-speed target detection based on the frequency-domain deramp-Keystone transform," *IEEE J. Sel. Topics Appl. Earth Observ. Remote Sens.*, vol. 9, no. 1, pp. 285–294, Jan. 2016.
[24] J. Xu, X.-G. Xia, S.-B. Peng, J. Yu, Y.-N. Peng, and L.-C. Qian, "Radar maneuvering target motion estimation based on generalized Radon-Fourier transform," *IEEE Trans. Signal Process.*, vol. 60, no. 12, pp. 6190–6201, Dec. 2012.
[25] J. Yu, J. Xu, Y. N. Peng, and X. G. Xia, "Radon-Fourier transform for radar target detection (iii): Optimality and fast implementations," *IEEE Trans. Aerosp. Electron. Syst.*, vol. 48, no. 2, pp. 991–1004, Apr. 2012.
[26] J. Xu *et al.*, "Adaptive radonfourier transform for weak radar target detection," *IEEE Trans. Aerosp. Electron. Syst.*, vol. 54, no. 4, pp. 1641–1663, Aug. 2018.
[27] J. C. Chen and R. E. Hudson, "Source localization and beamforming," *IEEE Signal Process. Mag.*, vol. 19, no. 2, pp. 30–39, Mar. 2002.
[28] J. Zhu, Q. Zhang, P. Gerstoft, M.-A. Badiu, and Z. Xu, "Grid-less variational bayesian line spectral estimation with multiple measurement vectors," *Signal Process.*, vol. 161, pp. 155–164, 2019. [Online]. Available: https://www.sciencedirect.com/science/article/pii/S0165168419301173
[29] M. Badiu, T. L. Hansen, and B. H. Fleury, "Variational Bayesian inference of line spectra," *IEEE Trans. Signal Process.*, vol. 65, no. 9, pp. 2247–2261, Sep. 2017.
[30] J. Zhu, L. Han, R. S. Blum, and Z. Xu, "Multi-snapshot newtonized orthogonal matching pursuit for line spectrum estimation with multiple measurement vectors," *Signal Process.*, vol. 165, pp. 175–185, 2019. [Online]. Available: https://www.sciencedirect.com/science/article/pii/S0165168419302658
[31] H. Wang and M. Kaveh, "Coherent signal-subspace processing for the detection and estimation of angles of arrival of multiple wide-band sources," *IEEE Trans. Acoust., Speech, Signal Process.*, vol. ASSP-33, no. 4, pp. 823–831, Aug. 1985.
[32] H. Hung and M. Kaveh, "Focussing matrices for coherent signal-subspace processing," *IEEE Trans. Acoust., Speech, Signal Process.*, vol. 36, no. 8, pp. 1272–1281, Aug. 1988.
[33] T. G. Kolda and B. W. Bader, "Tensor decompositions and applications," *SIAM Rev.*, vol. 51, no. 3, pp. 455–500, 2009.
[34] D. Oh and J. H. Lee, "Low-complexity range-azimuth FMCW radar sensor using joint angle and delay estimation without SVD and EVD," *IEEE Sensors J.*, vol. 15, no. 9, pp. 4799–4811, Sep. 2015.
[35] S. Kim, D. Oh, and J. Lee, "Joint DFT-ESPRIT estimation for TOA and DOA in vehicle FMCW radars," *IEEE Antennas Wireless Propag. Lett.*, vol. 14, pp. 1710–1713, 2015.
[36] R. A. Horn and C. R. Johnson, *Matrix Analysis*, 2nd ed. New York, NY, USA: Cambridge Univ. Press, 2012.
[37] J. A. Nelder and R. Mead, "A simplex method for function minimization," *Comput. J.*, vol. 7, no. 4, pp. 308–313, 1965.
[38] Z.-S. Liu and J. Li, "Implementation of the RELAX algorithm," *IEEE Trans. Aerosp. Electron. Syst.*, vol. 34, no. 2, pp. 657–664, Apr. 1998.
[39] Y. Jiao, J. Yu, and R. Che, "Application of RELAX algorithm to ISAR superresolution imaging," in *Proc. CIE Int. Conf. Radar*, Oct. 2006, pp. 1–4.
[40] J. Li, P. Stoica, and D. Zheng, "Angle and waveform estimation in the presence of colored noise via RELAX," in *Proc. Asilomar Conf. Signals, Syst. Comput.*, Oct. 1995, vol. 1, pp. 433–437.
[41] S. Lin, Y. Rong, X. Sun, and Z. Xu, "Learning capability of relaxed greedy algorithms," *IEEE Trans. Neural Netw. Learn. Syst.*, vol. 24, no. 10, pp. 1598–1608, Oct. 2013.
[42] Y. Zhang, "Super-resolution passive ISAR imaging via the RELAX algorithm," in *Proc. Int. Symp. Comput. Intell. Des.*, vol. 2, Dec. 2016, pp. 65–68.
[43] N. Jiang and J. Li, "Multiple moving target feature extraction for airborne HRR radar," *IEEE Trans. Aerosp. Electron. Syst.*, vol. 37, no. 4, pp. 1254–1266, Oct. 2001.
[44] G. H. Golub and C. F. van Loan, *Matrix Computations*, 4th ed. Baltimore, MD, USA: The Johns Hopkins Univ. Press, 2013.
[45] P. Stoica and R. L. Moses, *Spectral Analysis of Signals*. Upper Saddle River, NJ: Pearson/Prentice Hall, 2005.